

CM²



MAGAZINE

第 59 期



南方科技大学海洋磁学中心主编

<https://cm2.sustech.edu.cn/>

创刊词

海洋是生命的摇篮，是文明的纽带。地球上最早的生命诞生于海洋，海洋里的生命最终进化成了人类，人类的文化融合又通过海洋得以实现。人因海而兴。

人类对海洋的探索从未停止。从远古时代美丽的神话传说，到麦哲伦的全球航行，再到现代对大洋的科学钻探计划，海洋逐渐从人类敬畏崇拜幻想的精神寄托演变成可以开发利用与科学研究的客观存在。其中，上个世纪与太空探索同步发展的大洋科学钻探计划将人类对海洋的认知推向了崭新的纬度：深海（deep sea）与深时（deep time）。大洋钻探计划让人类知道，奔流不息的大海之下，埋藏的却是亿万年的地球历史。它们记录了地球板块的运动，从而使板块构造学说得到证实；它们记录了地球环境的演变，从而让古海洋学方兴未艾。

在探索海洋的悠久历史中，从大航海时代的导航，到大洋钻探计划中不可或缺的磁性地层学，磁学发挥了不可替代的作用。这不是偶然，因为从微观到宏观，磁性是最基本的物理属性之一，可以说，万物皆有磁性。基于课题组的学科背景和对海洋的理解，我们对海洋的探索以磁学为主要手段，海洋磁学中心因此而生。

海洋磁学中心，简称 CM^2 ，一为其全名“Centre for Marine Magnetism”的缩写，另者恰与爱因斯坦著名的质能方程 $E = MC^2$ 对称，借以表达我们对科学巨匠的敬仰和对科学的不懈追求。

然而科学从来不是单打独斗的产物。我们以磁学为研究海洋的主攻利器，但绝不仅限于磁学。凡与磁学相关的领域均是我们关注的重点。为了跟踪反映国内外地球科学特别是与磁学有关的地球科学领域的最新研究进展，海洋磁学中心特地主办 CM^2 Magazine，以期与各位地球科学工作者相互交流学习、合作共进！

“海洋孕育了生命，联通了世界，促进了发展”。21世纪是海洋科学的时代，由陆向海，让我们携手迈进中国海洋科学的黄金时代。

目 录

文献速递

1. 与深度有关的橄榄岩-熔体相互作用及克拉通地幔中不同硅含量的来源... 1
2. 微生物岩作为古地磁记录载体的可行性研究..... 3
3. 新仙女木-全新世时期劳伦冰盖南部的冰川年代学..... 7
4. 树轮记录的放射性碳揭示了过去千年中的太阳 11 年周期..... 11
5. 峨眉山大火成岩省岩浆期：来自越南北部记录..... 14
6. 考古烧制粘土和砖中的高矫顽力磁性矿物..... 16
7. 年龄校正地层的物源演化揭示了华南地块与冈瓦纳碰撞的时间和方式... 18
8. 中国黄土高原西南部邛山黄土-古土壤序列高分辨率元素结果揭示的过去 260 ka 千年尺度夏季风波动..... 20
9. 近 2000 年来 ENSO-SAM 对南极海冰范围数十年尺度上趋势的影响..... 23
10. SCHA. DIF. 4k: 重建欧洲 4 kyr 以来的地磁场变化及其在测年中的应用... 28
11. 茶马古道历史的社会韧性及其尺度效应..... 31
12. 高温下磁铁矿、磁黄铁矿、赤铁矿的磁滞特征..... 33
13. 赤道太平洋 E-O 转换期间生产力变化..... 36

1. 与深度有关的橄榄岩-熔体相互作用及克拉通地幔中不同硅含量的来源



翻译人：冯婉仪 fengwy@sustech.edu.cn

Tomlinson E L, Kamber B S. *Depth-dependent peridotite-melt interaction and the origin of variable silica in the cratonic mantle* [J]. *Nature Communications*, 2021, 12:1082.

<https://doi.org/10.1038/s41467-021-21343-9>

摘要：来自太古代克拉通厚根部的橄榄岩以其组成多样性而闻名，并且这些橄榄岩的起源仍有争议。我们报道了橄榄岩与上升地幔熔体之间反应的热力学模拟结果。极富镁的熔体（科马提岩）和橄榄岩之间的反应导致斜方辉石结晶，从而生成富硅的方辉橄榄岩。相比之下，浅部玄武质熔体-橄榄岩反应导致橄榄石富集，生成不能通过简单熔融产生的富镁纯橄榄岩。科马提岩在时空上与太古代地体中的玄武岩相关，这表明中度熔融与高度熔融并存的特征。我们设想一个相对较冷的地幔经历了间歇性的热物质上涌，如果新生克拉通的根部发生局部的强烈伸展，这两种熔融环境可能共存。另一种可能是，在克拉通合并之前，深部难熔的富硅残余体可能已从较浅的纯橄质岩石圈分离出来。不管怎么样，不同的太古代熔融反应环境共同造就了克拉通岩石圈的斜向和多模态的橄榄石分布和地表的双峰式镁铁质-超镁铁质火山活动。

ABSTRACT: Peridotites from the thick roots of Archaean cratons are known for their compositional diversity, whose origin remains debated. We report thermodynamic modelling results for reactions between peridotite and ascending mantle melts. Reaction between highly magnesian melt (komatiite) and peridotite leads to orthopyroxene crystallization, yielding silica-rich harzburgite. By contrast, shallow basalt-peridotite reaction leads to olivine enrichment, producing magnesium-rich dunites that cannot be generated by simple melting. Komatiite is spatially and temporally associated with basalt within Archaean terranes indicating that modest-degree melting co-existed with advanced melting. We envisage a relatively cool mantle that experienced episodic hot upwellings, the two settings could have coexisted if roots of nascent cratons became locally strongly extended. Alternatively, deep refractory silica-rich residues could have been detached from shallower dunitic lithosphere prior to cratonic amalgamation.

Regardless, the distinct Archaean melting-reaction environments collectively produced skewed and multi-modal olivine distributions in the cratonic lithosphere and bimodal mafic-ultramafic volcanism at surface.

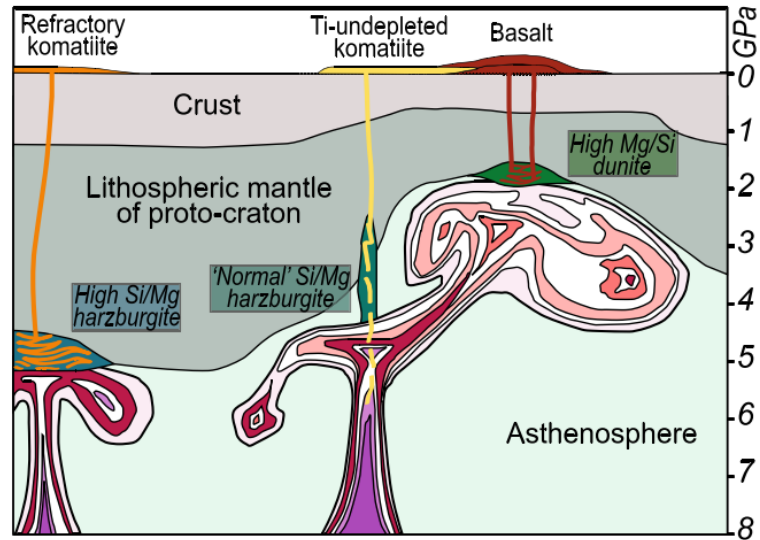


Figure 1. Schematic diagram showing three main mantle melting zones of a growing craton (vertically exaggerated). The proto-cratonic lithosphere is thick on left-hand side but strongly extended on right-hand side. Two hot mantle upwellings are shown. On the left, the upwelling encounters strong refractory harzburgite and komatiite-harzburgite reaction forms new komatiite and residual orthopyroxene-rich, low MgO/SiO₂ harzburgite. In the centre, an upwelling asymmetrically impinges on the extended lithosphere. Within the root of the upwelling, polybaric melting of asthenosphere forms non-depleted komatiite. In the diverted expanding head, basalt is produced, reacting with pre-existing shallow harzburgite to form more basalt and residual high MgO/SiO₂ dunite.

2. 微生物岩作为古地磁记录载体的可行性研究



翻译人:李园洁 liyj3@sustech.edu.cn

Jung J-I and Bowles JA, A Feasibility Study of Microbialites as Paleomagnetic Recorders [J].

Front. Earth Sci. 2021, 9:603805.

<http://doi.org/10.3389/feart.2021.603805>

摘要: 层状生物沉积物-微生物岩存在地质记录中,并可追溯到古老的时间,比如估计的内核成核时间。微生物岩由于高生长率可能保存高分辨率的地磁场变化记录。前人的研究表明微生物岩具有稳定的磁化强度,但是微生物岩磁化强度的形成时间和根源并不清楚,也没有评估快速生长的微生物岩是否能记录到地磁场的研究。本文,作者展示了美国大盐湖(Great Salt Lake)和墨西哥拉古纳巴拉卡拉(Laguna Bacalar)的现代微生物岩,大盐湖的更新世微生物岩和蒙古的寒武纪微生物岩结构中的厘米级磁化强度和磁学性质的变化。所有的样品记录到的磁场方向接近预计值。主要的载磁矿物具有 35-50 mT 矫顽力,解阻温度接近磁铁矿。一小部分是高矫顽力的矿物如赤铁矿,但对天然剩磁没有明显的贡献。沿着微生物岩层的磁化强度基本一致,方向的变化与微生物岩层的内部斜率相关。这些结果表明记录到的天然剩磁可能主要是碎屑成因,磁化强度获得时间接近沉积物沉积时间。

ABSTRACT: Microbialites-layered, organosedimentary deposits-exist in the geologic record and extend back in deep time, including all estimated times of inner core nucleation. Microbialites may preserve magnetic field variations at high-resolution based on their estimated growth rates. Previous studies have shown that microbialites can have a stable magnetization. However, the timing and origin of microbialite magnetization were not well determined, and no study has attempted to evaluate whether actively growing microbialites record the geomagnetic field. Here, we present centimeter-scale magnetization and magnetic property variations within the structure of modern microbialites from Great Salt Lake (GSL), United States, and Laguna Bacalar, Mexico, Pleistocene microbialites from GSL, and a Cambrian microbialite from Mongolia. All samples record field directions close to the expected value. The dominant magnetic carrier has a coercivity of 35-50 mT

and unblocking temperatures are consistent with magnetite. A small proportion of additional high coercivity minerals such as hematite are also present, but do not appear to appreciably contribute to the natural remanent magnetization (NRM). Magnetization is broadly consistent along microbialite layers, and directional variations correlate with the internal slope of the layers. These observations suggest that the documented NRM may be primarily detrital in origin and that the timing of magnetization acquisition can be close to that of sediment deposition.

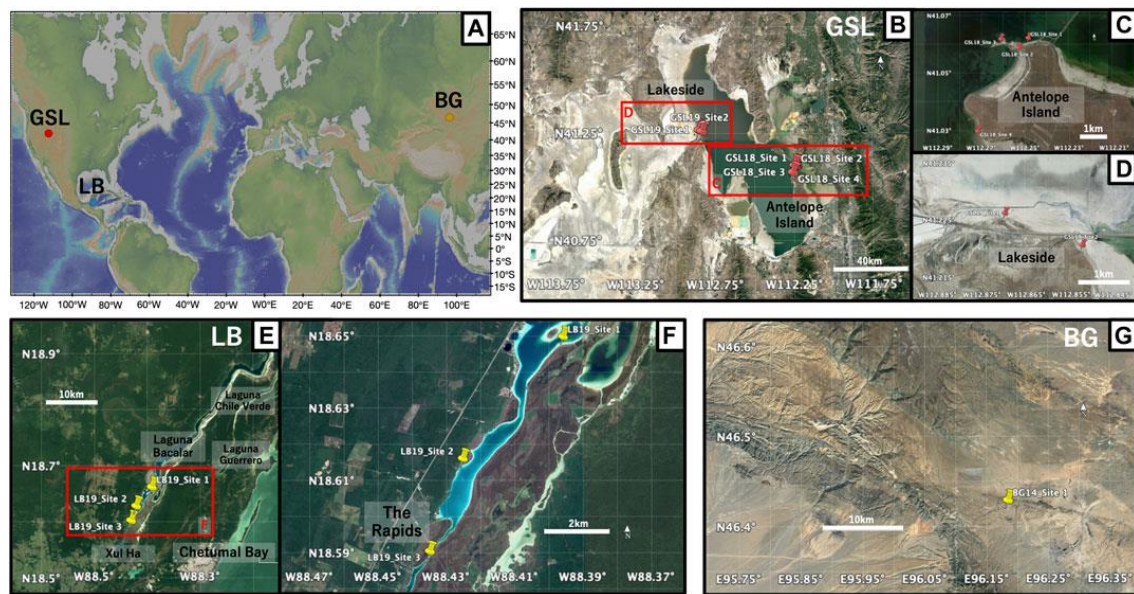


Figure 1. (A) Global map of the locations of three microbialite samples: Great Salt Lake (GSL), Utah; Laguna Bacalar (LB), Quintana Roo, MX; Bayan Gol formation (BG), Southwestern Mongolia. The figure was made with GeoMapApp (www.geomapapp.org) (Ryan et al., 2009). (B) Satellite image of the sampling locations of microbialites at GSL (C) Close-up of GSL18 study localities at the Antelope Island and (D) GSL 19 sampling sites at Lakeside. (E) Satellite image of sampling locations of microbialites at LB. (F) Close-up of LB19 study localities and three sampling sites. (G) Satellite image of sampling locations at BG. Imagery from July 2019 for GSL, april 2018 for LB, and april 2019 for BG, ©2019 Google, Image Landsat/Copernicus.

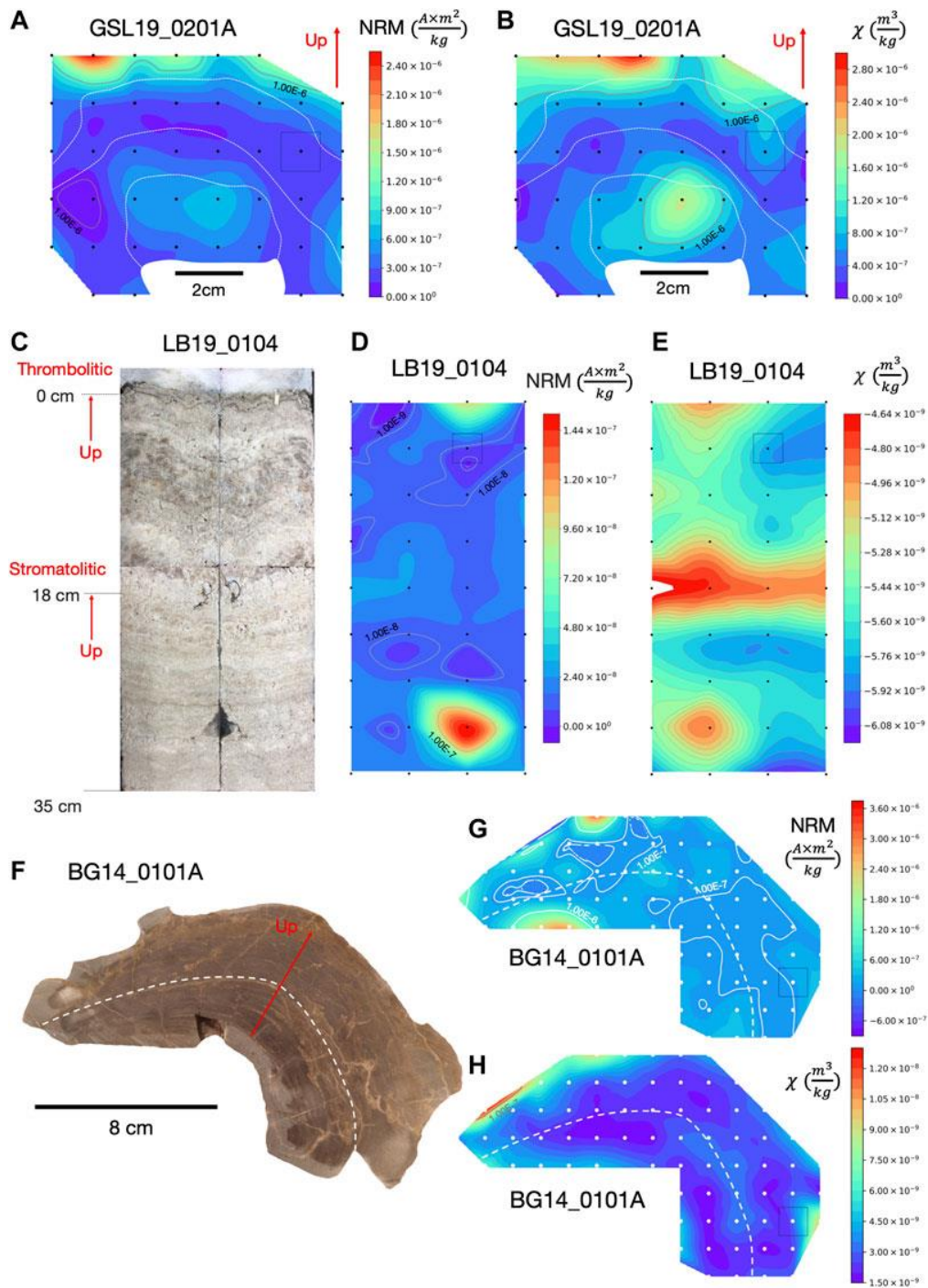


Figure 2. NRM intensity and magnetic susceptibility maps of microbialites with cubic interpolation to produce contours. (A) NRM intensity map and (B) magnetic susceptibility map of GSL19_0201A with approximate 1.5 cm spatial resolution. (C) Photo of split large push core (LB19_0104) from unlithified living microbialite with stromatolitic structures laminations up to 18 cm and thrombolitic structures from 18 cm to the top. (D) NRM intensity map and (E) magnetic susceptibility map of LB19_0104 with approximate 3.5 cm spatial resolution. (F) Photograph of BG14_0101 sample slice prior to sub-sampling,

and (G) its NRM intensity map and (H) magnetic susceptibility map with approximate 1 cm spatial resolution. Color contours are on a linear scale but labeled gray contour lines show order of magnitude variations. Black or white dots are sample positions and the color bars represent NRM intensity (Am^2/kg) and magnetic susceptibility (m^3/kg) values in the color range. Gray squares illustrate approximate specimen sizes on sample maps. Solid (up) red arrow indicates up in the field and is similar to the sample growth direction. White dashed lines roughly represent locations of distinct laminations. The red arrow represents the up direction in the field, which is close to the growth direction.

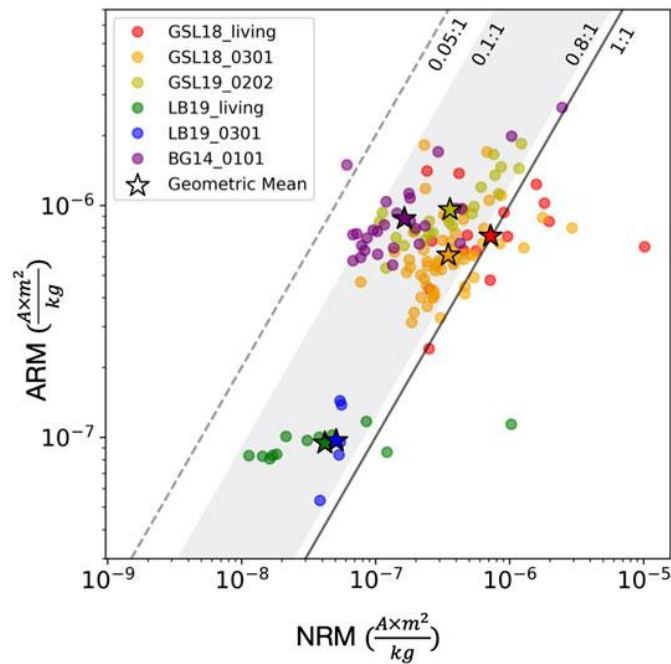


Figure 3. NRM intensity (x-axis) vs. ARM intensity (y-axis) of microbialites on log scales. The sample group of GSL18_living (GSL18 living microbialites with cyanobacteria layer collected from Antelope Island Site 1, 2 and 4), GSL18_0301 (lithified microbialite from Antelope Island Site 3), GSL19_0202 (lithified modern microbialite from Lakeside Site 2), LB19_living (surface living microbialite samples collected from LB19 Site 1 and 3), LB19_0301 (lithified porous microbialite sample from LB19 Site 3), BG14_0101 (Cambrian Bayan Gol formation stromatolite) are shown with red, orange, yellow, green, blue, and purple circles, and their geometric means are symbolized with stars. The black solid line represents NRM to ARM ratio of 1 ($x = y$), and measurements plotted on the left side of this line ($\text{ARM} \gg \text{NRM}$) is consistent with a DRM origin. The gray shading shows the NRM/ARM range of clastic sediments (0.1–0.8) (e.g., Levi and Banerjee, 1976; Constable, 1985), and the gray dashed line represents the maximum constraint for biogenic magnetite (0.05) (e.g., Roberts et al., 2012; Rodelli et al., 2019).

3. 新仙女木-全新世时期劳伦冰盖南部的冰川年代学



翻译人：仲义 zhongyi@sustech.edu.cn

Breckenridge, A., Lowell T.V., Peteet, D., A new glacial varve chronology along the southern Laurentide Ice Sheet that spans the Younger Dryas-Holocene boundary [J]. Geology, 2020, 49(3), 283-288.

<https://doi.org/10.1130/G47995.1>

摘要：冰期纹泥能够细节性指示冰川边缘位置，并提供相比于格陵兰冰芯记录相比同样高分辨率的淡水输入信息，因此，它可以成为评估古代和现代冰原对气候变化响应的关键性古记录。本文作者首次报道了北美地区跨越新仙女木事件(YD)-全新世边界(11.65 ka. B.P.)之间1500年的纹泥年代。这一年代依据的是加速质谱仪放射性¹⁴C测定的陆生大型化石，这些化石主要分布在苏必利尔湖盆地洪水时期沉积的广泛的红黏土层底部。我们通过研究晚新仙女木事件时期和全新世边界的冰缘后退和融化来说明这一记录的效用。冰缘后撤的速率恒定，发生在晚新仙女木时期和全新世开始之后的300年。相反，在边界处，纹层厚度增加，冰碛形成超过50年，这可能是气候变暖的响应。作者期望通过这个时间序列的发展和完善，有望成为北美最长、地理范围最广的冰川纹泥数据库。

ABSTRACT: Glacial varves can detail ice-margin positions and provide a proxy for meltwater discharge at resolutions comparable to those of the Greenland ice core archives, and thus they can be critical paleorecords for assessing the response of both ancient and modern ice sheets to climate change. Here we provide an ~1500 yr varve chronology straddling the Younger Dryas (YD)–Holocene boundary (11.65 cal. kyr B.P.), the first such chronology in North America. The varves are from glacial Lake Agassiz (central North America). The chronology is pinned on accelerator mass spectrometry radiocarbon-dated terrestrial macrofossils at the base of a widespread red-clay bed deposited during flooding from the Lake Superior basin. We illustrate the utility of this record by examining ice-margin retreat and melting through the late Younger Dryas and across the Holocene boundary. The ice margin receded at a constant rate, not only during the late YD, but for at least 300 yr after the onset of the Holocene. In contrast, varve thicknesses increased at the

boundary, and a moraine formed over a 50 yr period, perhaps in response to the warming climate. Our expectation is that this time series will continue to be developed, expanded, and refined because it promises to be the longest and most geographically extensive glacial varve data set in North America.

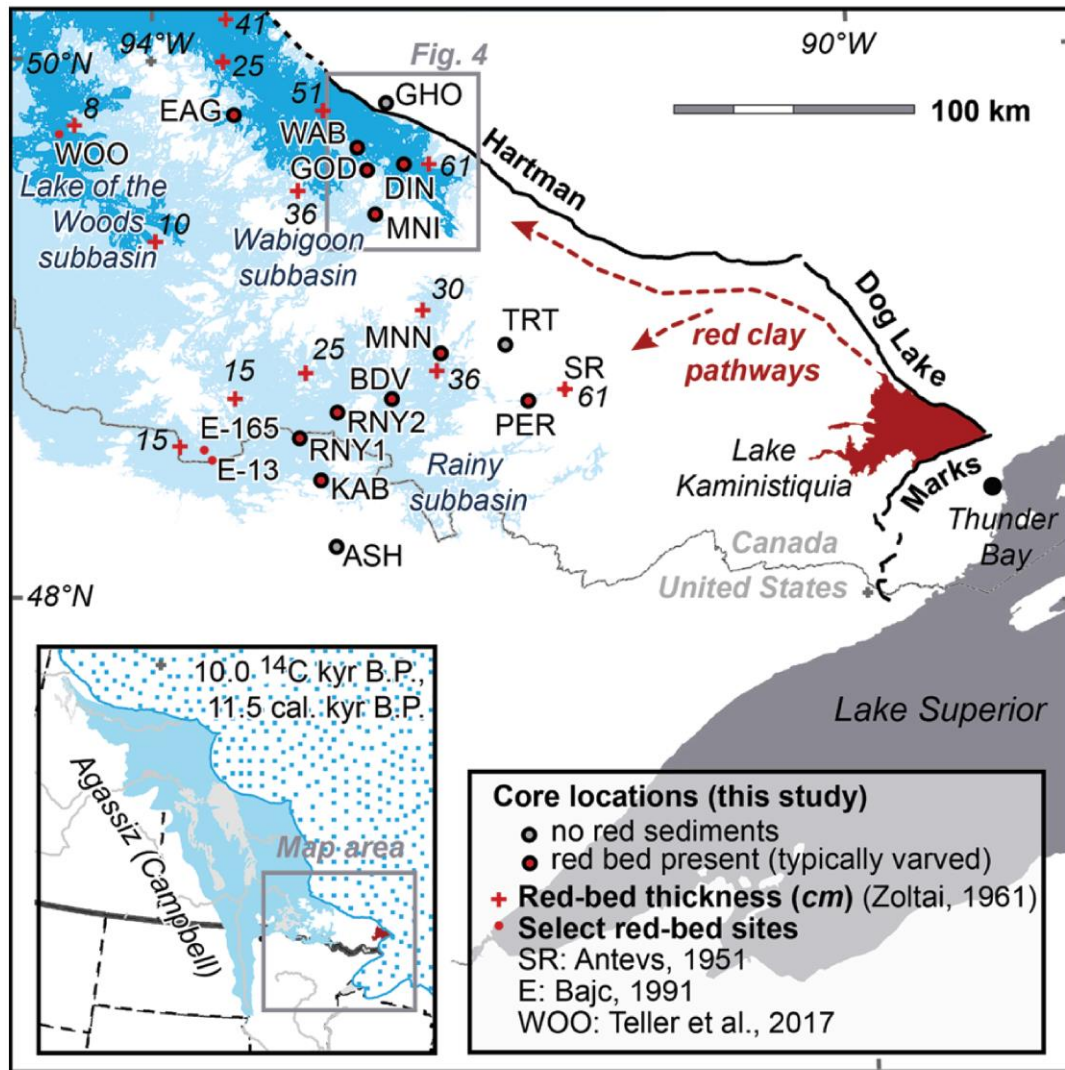


Figure 1. Red-bed sites and thickness (in cm) associated with glacial Lake Agassiz (central North America). Lake Agassiz levels from Breckenridge (2015) are shown: lowest Moorhead (medium blue) and Campbell (light blue). White indicates areas not covered by Lake Agassiz at these levels, but must have included extensive lakes. Red clay is from glacial Lake Kaministiquia. Black lines trace correlative Hartman, Dog Lake, and Marks moraines. Inset map shows the 10,000 ¹⁴C yr B.P. ice margin from Dalton et al. (2020).

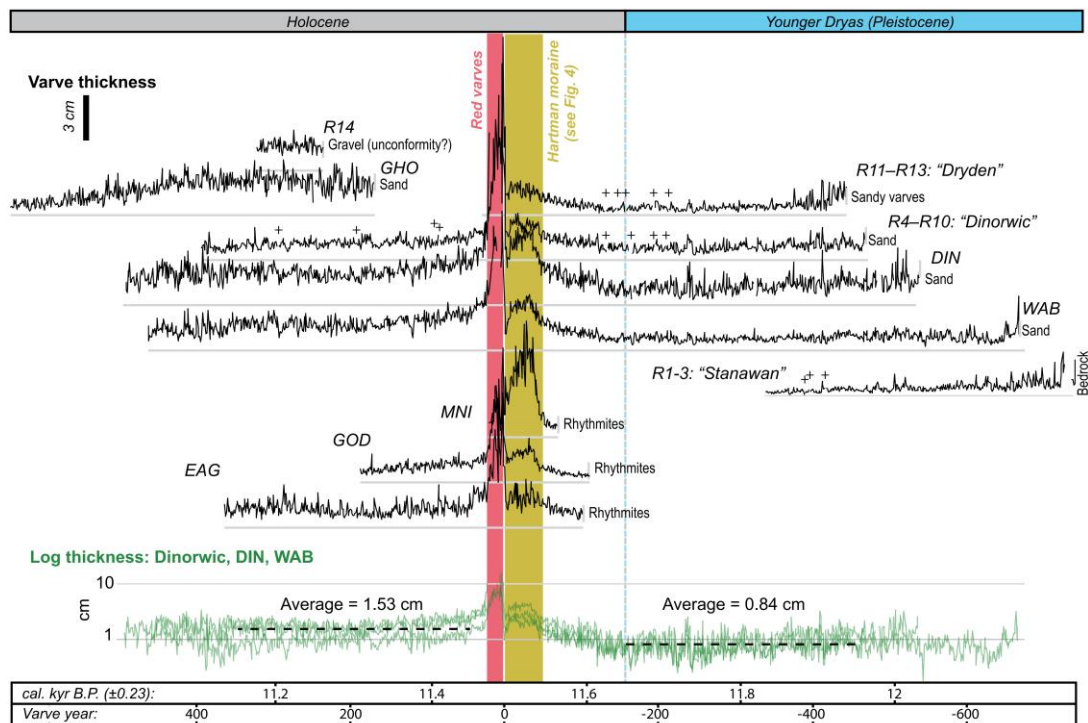


Figure 2. Wabigoon subbasin (glacial Lake Agassiz, central North America) varve thickness data (younger to left; see Fig. 1 for site locations). Red varve onset (varve year 1) is ^{14}C dated at site PER to 11.49 ± 0.23 cal. kyr B.P. (thousands of calibrated years before A.D. 1950). Rittenhouse (1933) series are stacked from multiple sites (Fig. 4, sites R1–R14), and cross symbols identify missing varves relative to our core records. At sites MNI, GOD, and EAG, below the red varves are rhythmites, which transition to a lower varve series. Correlating these older varves to the Rainy subbasin is work in progress, but core logs are provided in the Supplemental Material (see footnote 1). Note the 3 cm varve thickness scale, except for the green data plotted on a log scale to highlight the thickness increases at the Younger Dryas–Holocene transition. Association of the Hartman moraine with thicker varves shaded yellow is explained in the text.

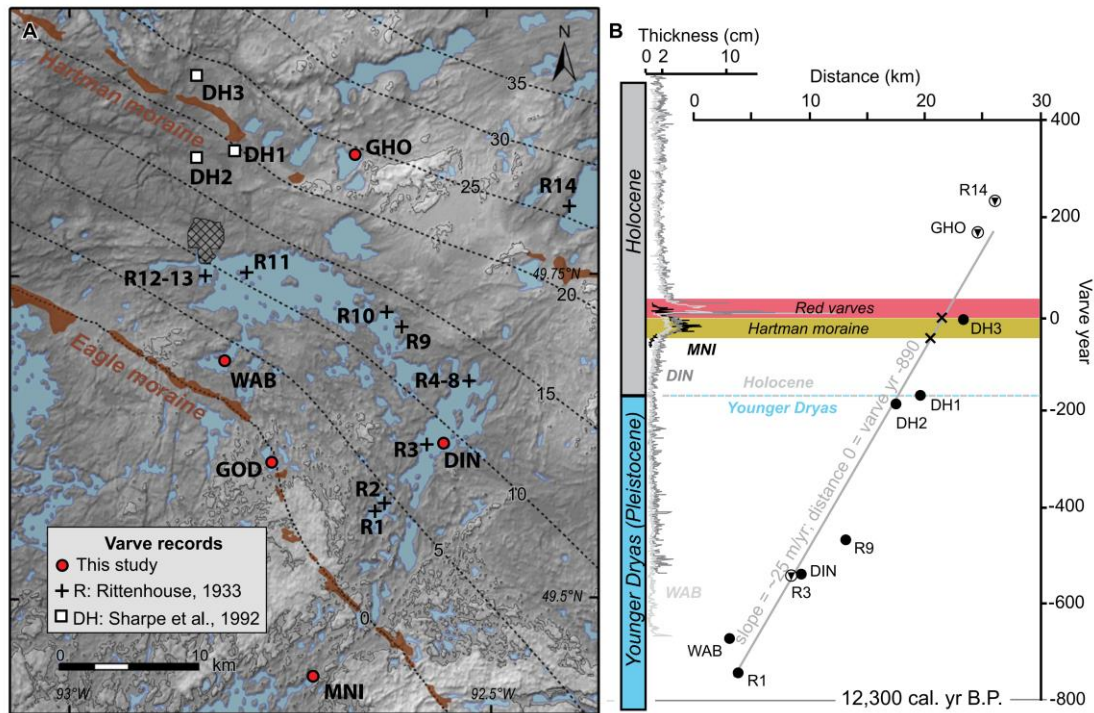


Figure 3. (A) Varve sites on a hillshade digital elevation model (using Shuttle Radar Topography Mission data) and moraines mapped by Cowan and Sharpe (1991). Eagle-Hartman moraine spacing increases from 21 to 35 km across this area, therefore distance contours were constructed by forcing distance to a constant 21 km. Contours (labeled in km) mimic inferred ice-margin positions and provide a means to compare relative distances for each site to the Eagle moraine (distance = 0). (B) Ice-margin time-distance plot constructed from sites with basal varves (solid circles) or ice-proximal varves (circled triangles). Linear regression for these data is in gray. Cross symbols hypothetically associate the northern and southern edges of the Hartman moraine with the first and last of the series of anomalously thick varves between varve years -50 and -1 (see Fig. 3 for explanation of varve years). cal. yr B.P.—calibrated years before A.D. 1950.

4. 树轮记录的放射性碳揭示了过去千年中的太阳 11 年周期



翻译人：柳加波 liujb@sustech.edu.cn

Brehm N, Bayliss A, Christl M, et al. **Eleven-year solar cycles over the last millennium revealed by radiocarbon in tree rings** [J]. *Nature Geoscience*, 2021, 14(1): 10-15.

<https://doi.org/10.1038/s41561-020-00674-0>

摘要：太阳是地球的主要能量来源。太阳活动是气候变化的重要外部驱动力。我们对太阳黑子活动的观测仅有 400 多年历史。对于太阳活动在更久远的历史上的变化，则可以通过宇宙射线产生的放射性核素进行重建。这些放射性核素能够保存在树轮和冰芯中长达数千年。但是，长时间尺度上精确定年的放射性核素记录受天气引起的噪声和低分辨率的限制，阻碍了对基于宇宙核素成因的短期太阳活动的研究，例如 11 年的 Schwabe 周期。本文，我们建立了一个连续的、年度分辨率的大气 ^{14}C 浓度（经分馏校正后的 $^{14}\text{CO}_2$ 与 CO_2 的比值）记录。该记录是从过去上千年中（AD 969 - 1933）有绝对定年的树轮中测量得到的。高分辨率和高精度的 ^{14}C 记录揭示了这段时间内 Schwabe 周期的存在。此外，该记录还确认了 AD 993 的太阳高能粒子事件，并揭示了两个可能的事件（AD 1052 和 AD 1279）。这表明对现代电子系统有害的强太阳事件可能比以前认为的发生得更频繁。高时间分辨率的大气放射性碳记录不仅显示了过去千年中十年尺度上的太阳活动，还为该时间段内更精确的放射性碳定年提供了有用的基准。

ABSTRACT: The Sun provides the principal energy input into the Earth system and solar variability represents a significant external climate forcing. Although observations of solar activity (sunspots) cover only the last about 400 years, radionuclides produced by cosmic rays and stored in tree rings or ice cores serve as proxies for solar activity extending back thousands of years. However, the presence of weather-induced noise or low temporal resolution of long, precisely dated records hampers cosmogenic nuclide-based studies of short-term solar variability such as the 11-yr Schwabe cycle. Here we present a continuous, annually resolved atmospheric ^{14}C concentration (fractionation-corrected ratio of $^{14}\text{CO}_2$ to CO_2) record reconstructed from absolutely dated tree rings covering nearly all of the last millennium (AD 969–1933). The high-resolution and precision ^{14}C record reveals the presence of the Schwabe cycle over the entire time range. The record confirms

the AD 993 solar energetic particle event and reveals two new candidates (AD 1052 and AD 1279), indicating that strong solar events that might be harmful to modern electronic systems probably occur more frequently than previously thought. In addition to showing decadal-scale solar variability over the last millennium, the high-temporal-resolution record of atmospheric radiocarbon also provides a useful benchmark for making radiocarbon dating more accurate over this interval.

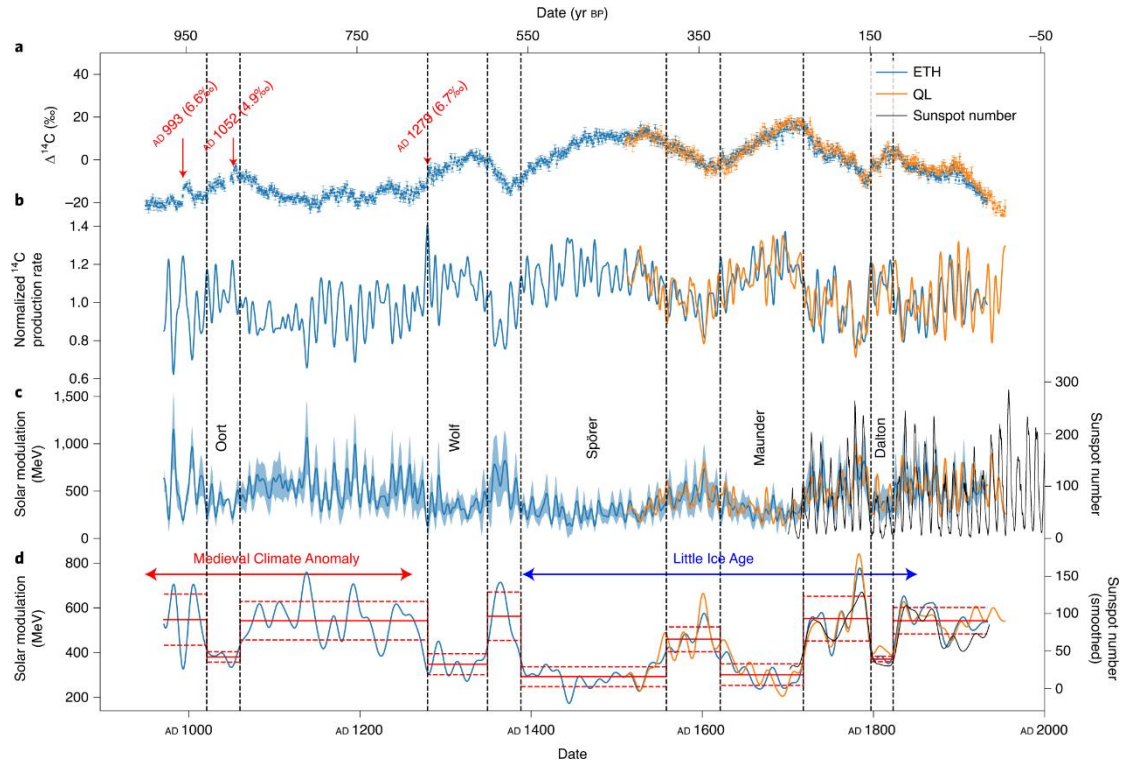


Figure 1. From annual $\Delta^{14}\text{C}$ records to solar modulation. **a**, Annual ETH and QL17 $\Delta^{14}\text{C}$ records with 2σ error bars. Red arrows indicate possible events, their respective date and $\Delta^{14}\text{C}$ increase. **b**, Normalized ^{14}C production rates calculated from ETH and QL data. **c**, Reconstructed solar modulation parameter Φ from ETH and QL ^{14}C production rates. The blue band indicates the uncertainty (in the ETH data) estimated by the Monte Carlo simulation. The international sunspot numbers (black, right y axis) are given for comparison. **d**, 20-yr low-pass-filtered Φ with mean values (ETH data, solid red lines) and the corresponding standard deviation (red dashed lines) for the different time periods. The 20-yr low-pass-filtered sunspot numbers (black, right y axis) are given for comparison. Vertical dashed black lines mark the beginnings and ends of grand solar minima.

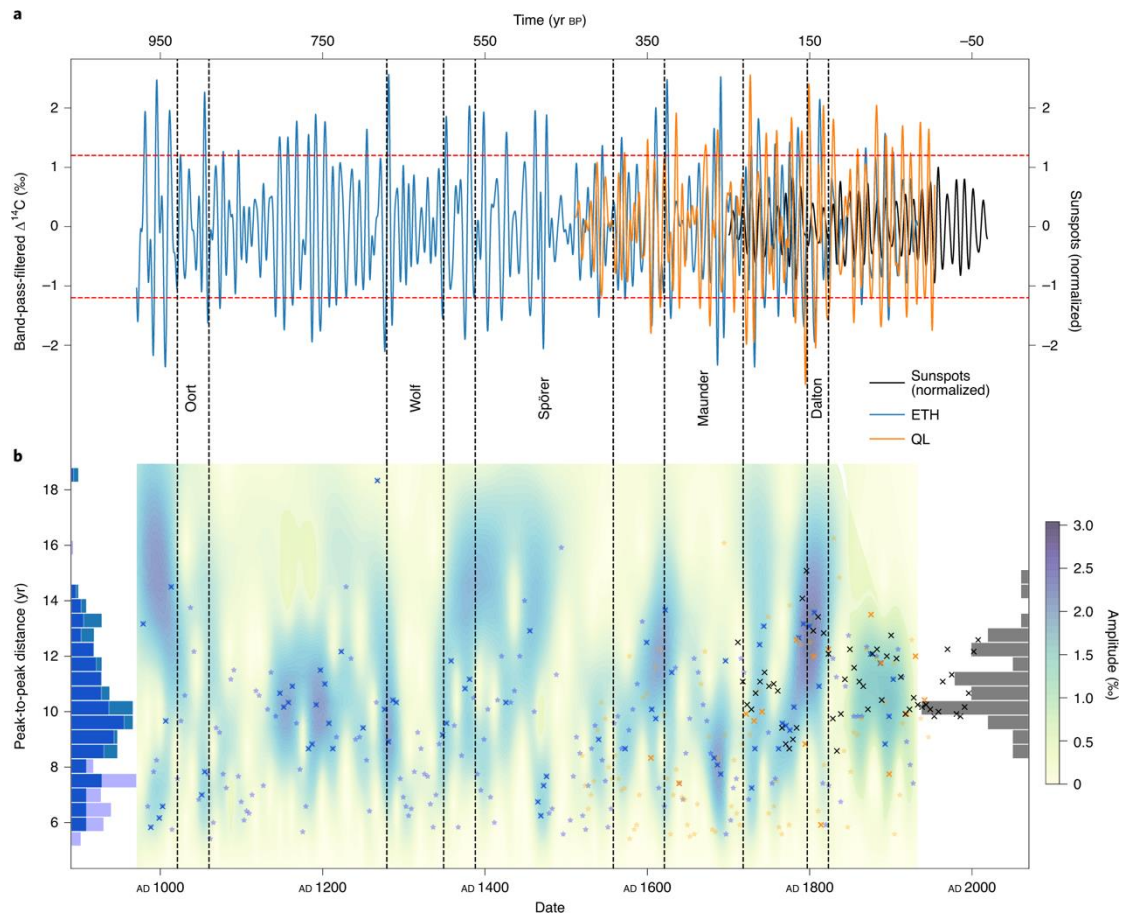


Figure 2. Frequency analysis of band-pass filtered $\Delta^{14}\text{C}$ records. a, 6- to 18-yr band-pass-filtered $\Delta^{14}\text{C}$ data and 1.2‰ significance level (red dashed lines). The band-pass-filtered and normalized sunspot record is shown in black. b, Morlet wavelet amplitude colour map of the band-pass-filtered ETH data. Data points indicate peak-to-peak distances of the band-pass-filtered $\Delta^{14}\text{C}$ records (light blue stars, ETH; light orange stars, QL; black crosses, sunspots). Blue and orange crosses mark the peak-to-peak distances for significant amplitudes (>1.2‰). The histograms on both sides show the distribution of period lengths for the sunspot numbers (black), all periods in the ETH data (light blue) and the significant periods only (dark blue). Vertical dashed black lines mark grand solar minima.

5. 峨眉山大火成岩省岩浆期：来自越南北部记录



翻译人：周洋 zhouy3@sustech.edu.cn

J. Gregory Shellnutt, Thuy Thanh Pham, Steven W. Denyszyn., et al. Magmatic duration of the Emeishan large igneous province: Insight from northern Vietnam [J]. Geology, 2020, 48: 457–461.

<https://doi.org/10.1130/G47076.1>

摘要：在中国西南部和越南北部喷发的峨眉山熔岩被认为是导致 Capitanian 期生物大灭绝和随后全球变冷事件的原因，但火山爆发的持续时间尚不确定。由于缺乏晚期火山岩高精度年龄数据，火山结束时间难以确定。在越南北部的 Tu Le 流纹岩是峨眉山大火成岩省（ELIP）中体积最大的硅质单元，在空间上与 Muong Hum 和 Phan Si Pan 浅成侵入体相连。Tu Le 流纹岩（ 257.1 ± 0.6 Ma 至 257.9 ± 0.3 Ma），Muong Hum（ 257.3 ± 0.2 Ma）和 Phan Si Pan（ 256.3 ± 0.4 Ma）产生了 ELIP 的最年轻的高精度年龄。结果表明，峨眉山熔岩爆发时间超过 6 m.y.，之后不久为岩浆侵位。因此，峨眉山的火山活动可能导致了全球在中 Wuchiapingian 期开始降温。这些岩石代表着 ELIP 岩浆作用的不同时期，它们很年轻，并侵位于南北向的 Panxi 裂谷。

ABSTRACT: The eruption of Emeishan lava in southwestern China and northern Vietnam is considered to be a contributing factor to the Capitanian mass extinction and subsequent global cooling event, but the duration of volcanism is uncertain. The difficulty in assessing the termination age is, in part, due to the lack of high-precision age data for late-stage volcanic rocks. The Tu Le rhyolite of northern Vietnam is the most voluminous silicic unit of the Emeishan large igneous province (ELIP) and is spatially associated with the Muong Hum and Phan Si Pan hypabyssal plutons. Chemical abrasion–isotope dilution–thermal ionization mass spectrometry U–Pb dating of zircons from the Tu Le rhyolite (257.1 ± 0.6 Ma to 257.9 ± 0.3 Ma) and Muong Hum (257.3 ± 0.2 Ma) and Phan Si Pan (256.3 ± 0.4 Ma) plutons yielded the youngest high-precision ages of the ELIP yet determined. The results demonstrate that Emeishan lavas erupted over a period of ~6 m.y., with plutonism ending shortly thereafter. Thus, it is possible that Emeishan volcanism contributed to

global cooling into the middle Wuchiapingian. It appears that these rocks represent a distinct period of ELIP magmatism, as they are young and were emplaced oblique to the main north-south-trending Panxi rift.

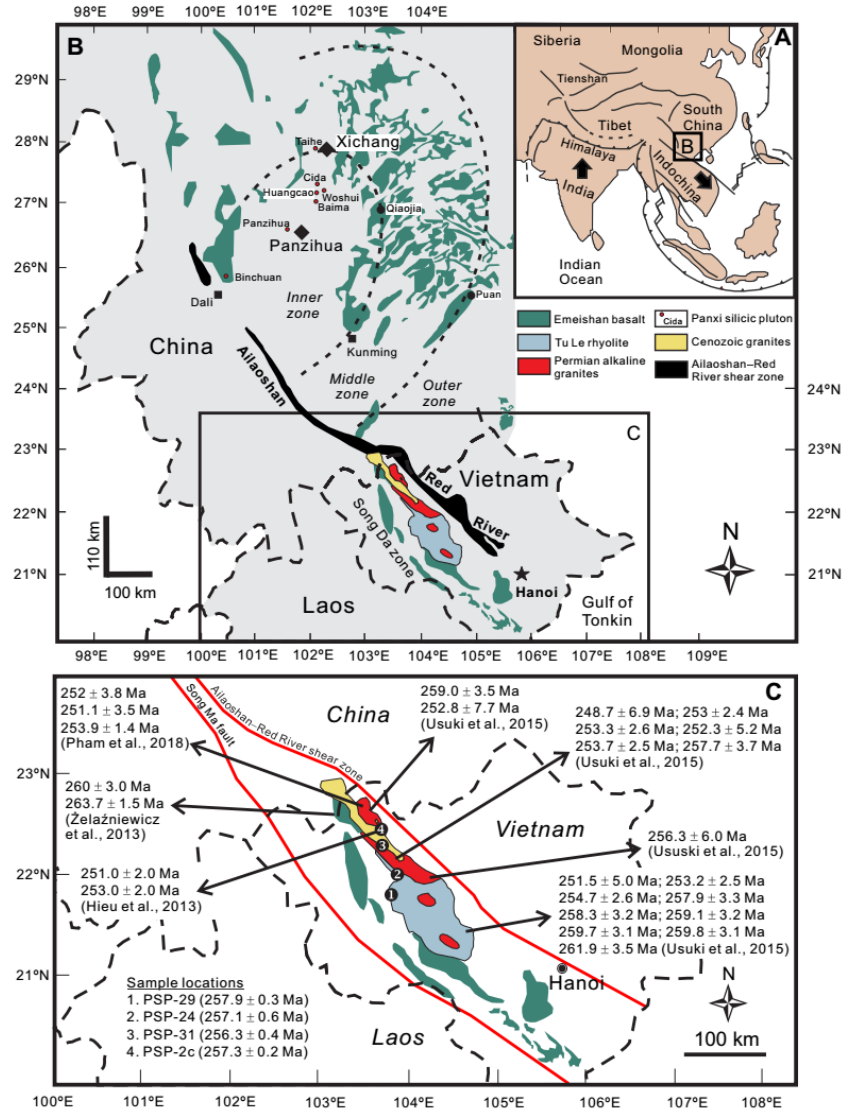


Figure 1. Map of the Emeishan large igneous province (ELIP), Ailaoshan-Red River shear zone, and Tu Le-Phan Si Pan region (southwestern China and northern Vietnam). (A) Inset map of major suture zones of eastern Asia. (B) Simplified map of the ELIP showing distribution of crustal zonation and position of main flood basalt relative to the displaced Tu Le-Phan Si Pan region. (C) Simplified geological map of the Tu Le-Phan Si Pan region with a summary of in situ zircon geochronology and sample locations for this study (locations 1–4). Other geochronology data are from Hieu et al. (2013), Zelaźniewicz et al. (2013), Usuki et al. (2015), and Pham et al. (2018).

6. 考古烧制粘土和砖中的高矫顽力磁性矿物



翻译人：曹伟 11930854@QQ.com

Andrei K , Mary K , Maria K A , et al. High-coercivity magnetic minerals in archaeological baked clay and bricks [J]. Geophysical Journal International, 2020, 224(2): 1257-1272.

<https://doi.org/10.1093/gji/ggaa508>

摘要：对磁性矿物的透彻理解是任何成功的古地磁或考古磁学研究的基础。考古陶瓷和烧结粘土中的磁性矿物可能是从原有材料中继承下来的，或者更常见的是在烧制过程中形成的。由此产生的磁性矿物可能很复杂，包括岩石中不常见的铁磁性类型。为此，我们对保加利亚和俄罗斯的一批具有代表性的考古陶瓷（燃烧结构和砖块的烘烤粘土）进行了详细的岩石磁性研究。实验包括测量温度在 20 °C 到 > 600 °C 之间的热退剩磁。对于选定的样品，在 1.8 到 300 K 之间进行了饱和剩磁和初始磁化率的低温测量。所有研究的样品都含有一种软磁性矿物，该矿物被鉴定为磁赤铁矿，可能被钛、锰和（或）铝所取代。样品中没有观察到化学计量的磁铁矿，这可以通过缺少 Verwey 转化来证明。此外，还发现了一种或两种硬磁性矿物，它们各自的解组温度有很大差异。在 540 °C 到 620 °C 之间，其中一种被认为是被取代的赤铁矿。另一种在较低的温度（140 °C 到 240 °C）下解组，其磁性对应于先前报告的神秘的高矫顽力、稳定的低解组温度（HCSLT）属性。在少数样品中，高温和低温解组的硬磁性矿物共存；在其他样品中，HCSLT 是唯一存在的硬磁矿物。

ABSTRACT: The thorough understanding of magnetic mineralogy is a prerequisite of any successful palaeomagnetic or archaeomagnetic study. Magnetic minerals in archaeological ceramics and baked clay may be inherited from the parent material or, more frequently, formed during the firing process. The resulting magnetic mineralogy may be complex, including ferrimagnetic phases not commonly encountered in rocks. Towards this end, we carried out a detailed rock magnetic study on a representative collection of archaeological ceramics (baked clay from combustion structures and bricks) from Bulgaria and Russia. Experiments included measurement of isothermal remanence acquisition and demagnetization as a function of temperature between 20 and >600 degrees C. For selected samples, low-temperature measurements of saturation remanence and initial magnetic susceptibility between 1.8 and 300 K have been carried out. All studied samples contain a

magnetically soft mineral identified as maghemite probably substituted by Ti, Mn and/or Al. Stoichiometric magnetite has never been observed, as evidenced by the absence of the Verwey phase transition. In addition, one or two magnetically hard mineral phases have been detected, differing sharply in their respective unblocking temperatures. One of these unblocking between 540 and 620 degrees C is believed to be substituted hematite. Another phase unblocks at much lower temperatures, between 140 and 240 degrees C, and its magnetic properties correspond to an enigmatic high coercivity, stable, low-unblocking temperature (HCSLT) phase reported earlier. In a few samples, high- and low unblocking temperature, magnetically hard phases appear to coexist; in the others, the HCSLT phase is the only magnetically hard mineral present.

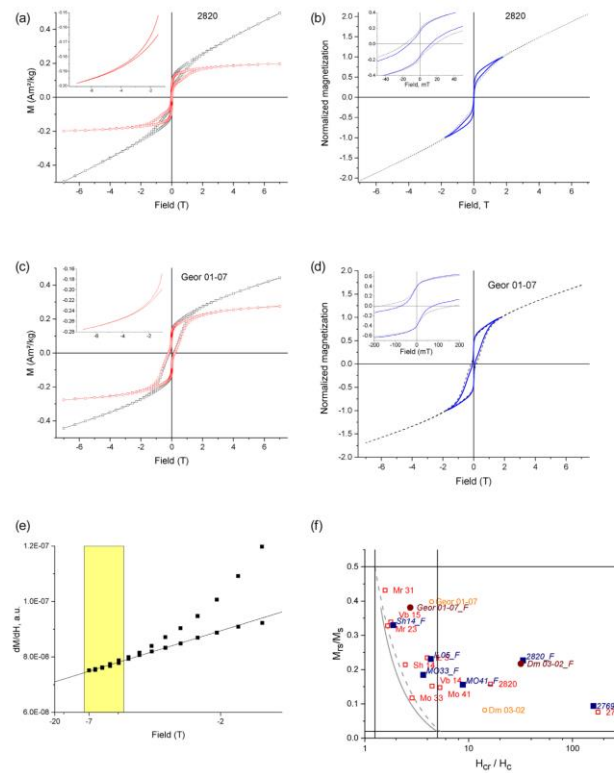


Figure 1. (a) Raw and corrected for high-field slope ± 7 T hysteresis loops for sample 2820, Bulgaria. Inset shows approach to saturation for the corrected loop. (b) A comparison of ± 7 T (dashed line) and ± 1.8 T (solid line) hysteresis loops for sample 2820. Magnetization is normalized to its value at the maximum field in the ± 1.8 T loop and to the magnetization value at 1.8 T on the ascending branch in the ± 7 T loop. Inset shows the ± 50 mT range to illustrate the effect of non-saturation on the coercive force. (c and d) Same as (a) and (b) but for sample Geor 01–07, Yaroslavl'. Inset shows the ± 200 mT range. (e) Illustration of correction for high-field susceptibility. Shaded rectangle shows the field range where the $dM/dH(1/H)$ dependence is approximated by a straight line. (f) The Day plot comparing the position of figurative points corresponding to ± 1.8 T (open squares) and ± 7 T (solid squares) hysteresis loops, respectively.

7. 年龄校正地层的物源演化揭示了华南地块与冈瓦纳碰撞的时间和方式



翻译人：刘伟 inewway@163.com

Yang Chuan, Li Xianhua, Li Zheng-xiang, et al. *Provenance Evolution of Age-Calibrated Strata Reveals When and How South China Block Collided With Gondwana [J]. Geophysical Research Letters*, 2020, 47(19).

<https://doi.org/10.1029/2020GL090282>

摘要：华南地块被认为是冈瓦纳大陆的组成部分，但关于其向冈瓦纳大陆增生的时间和过程存在争议，这主要是由于华南地块缺乏可靠的“泛非期”古地磁数据和构造岩浆记录。对华南地块西部埃迪卡拉纪-寒武系沉积岩的碎屑锆石进行了原位 U-Pb 年龄和 Hf-O 同位素综合分析，年龄峰值分别为 2.51、1.85、1.20、0.80 和 0.52 Ga。碎屑锆石年龄谱表明，华南地块在 0.56 ~ 0.54 Ga 发生了一次重大的构造转变，反映了华南-印支地块与印度西北部地块碰撞的开始。碰撞事件一直持续到早奥陶世，导致了华南-印支地块与东冈瓦纳北缘的缝合。

ABSTRACT: The South China Block (SCB) has been regarded by many as an integral part of Gondwana, but proposed timing and processes for its accretion to Gondwana vary and remain contentious, largely owing to the lack of reliable Pan-African age paleomagnetic data and tectono-magmatic records from the SCB. Integrated in situ U-Pb ages and Hf-O isotope analyses of detrital zircons from geochronologically well-calibrated Ediacaran-Cambrian sedimentary rocks of western SCB reveal age populations of 2.51, 1.85, 1.20, 0.80, and 0.52 Ga. Detrital zircon age spectra indicate a major tectonic transition for the SCB during 0.56 - 0.54 Ga, interpreted to reflect the beginning of the collision between SCB-Indochina and NW India blocks. The collisional event lasted until early Ordovician, leading to the suturing of the SCB-Indochina to the northern margin of East Gondwana.

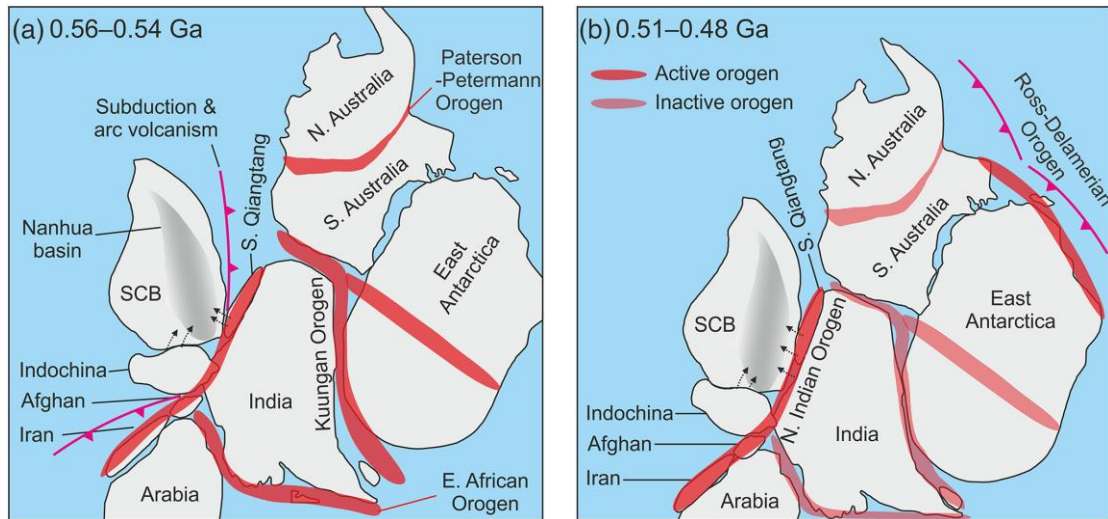


Figure 1. Paleogeographic reconstruction showing the assembly of East Gondwana during late (a) Ediacaran and (b) Cambro-Ordovician. Modified from Yao and Li (2016).

8. 中国黄土高原西南部邛山黄土-古土壤序列高分辨率元素结果揭示的过去 260 ka 千年

尺度夏季风波动

翻译人: 杨会会 11849590@mail.sustech.edu.cn



Wang Y, Guo F, Ma L et al. *Millennial-scale summer monsoon oscillations over the last 260 ka revealed by high-resolution elemental results of the Mangshan loess-palaeosol sequence from the southeastern Chinese Loess Plateau*[J]. *Quaternary International*, 2020,552,164-174
<https://doi.org/10.1016/j.quaint.2020.05.039>

摘要: 黄土指标已经被广泛应用于鉴别东亚季风冰期-间冰期尺度至千年尺度的变化。然而,黄土-古土壤序列中冰期-间冰期旋回中千年尺度变化的特征依然是不明确的。本文中,我们呈现了中国黄土高原西南部一个 96.7 米厚邛山黄土-古土壤序列的高分辨率(5 cm)地球化学元素结果,揭示出了其中的千年尺度季风变化。我们进行了黄土指标(磁化率、CaCO₃含量、Ca/K、Fe/K 和 Rb/Sr)和石笋氧同位素记录的时间序列分析,运用集成经验模态分解法将这些指标分解成了不同的组分。低频和高频组分的信号可以分别追索出季风在冰期-间冰期尺度及千年尺度上的变率。黄土指标千年尺度组分的占比在 9.4%~13.4%之间变化,少于中国石笋氧同位素记录的变率(~24.4%)。在黄土的 5 个指标中,Fe/K 是揭示千年尺度夏季风变化最敏感的指标,呈现出与中国石笋氧同位素记录近一致的突变变化。邛山记录的季风突变幅度在间冰期时比冰期时更大,这和古浪记录相一致,共同反映了黄土指标对冰期时弱风化现象的低敏感性和对间冰期时夏季风突变的放大作用。

ABSTRACT: Loess-based proxies have been widely used to infer glacial-interglacial to millennial-scale changes of the East Asian monsoon. However, the characteristic of millennial-scale variability is still unclear during glacial-interglacial cycles in loess-palaeosol sequence. Here, we present high-resolution (5-cm) elemental results of a 96.7-m thick Mangshan loess-palaeosol sequence on the southeastern Chinese Loess Plateau to emphasize millennial monsoon changes. We explore time series of loess proxies (magnetic susceptibility, CaCO₃ content, Ca/K, Fe/K, and Rb/Sr ratios) and

speleothem $\delta^{18}\text{O}$ records and decompose these proxies into intrinsic components using the ensemble empirical mode decomposition method. Synthesized signals of low- and high-frequency components can track the monsoon variability at glacial-interglacial and millennial timescales, respectively. The proportions of millennial components of the loess proxies vary from 9.4%~13.4%, less than that in Chinese speleothem $\delta^{18}\text{O}$ record (~24.4%). Among five loess proxies, Fe/K ratio is the most sensitive indicator of millennial-scale summer monsoon oscillations, exhibiting abrupt changes similar to that of the Chinese speleothem $\delta^{18}\text{O}$ record. The amplitude of abrupt monsoon changes recorded in Mangshan is larger during interglacials than glacials, which is in line with Gulang records, implying the lower sensitivity of loess proxies to weak weathering during glacial and an interglacial amplification of abrupt summer monsoon changes.

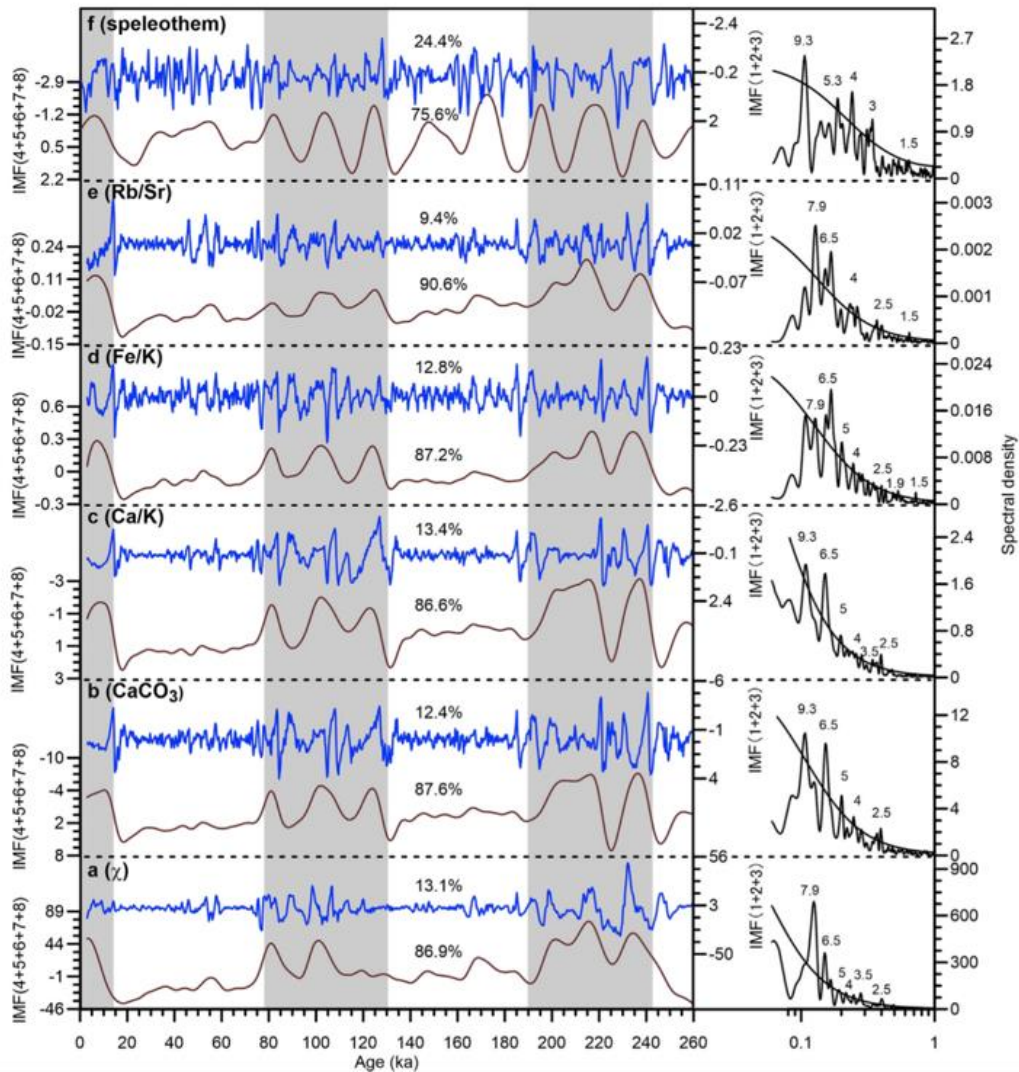


Figure 1. The relative contribution results of IMF (1+2+3) (blue, millennial components < 10-kyr) and IMF (4+5+6+7+8) (brown, glacial-interglacial components > 10-kyr) of magnetic susceptibility (a),

carbonate content (b), Ca/K (c), Fe/K (d), Rb/Sr (e) ratios and speleothem $\delta^{18}\text{O}$ (f) by EEMD method. Results of spectral analysis of millennial components shown on the right with numbers reveal dominant periodicities and dotted lines represent the 95% confidence level. Shaded bars indicate three interglacial periods (MIS 1, 5 and 7).

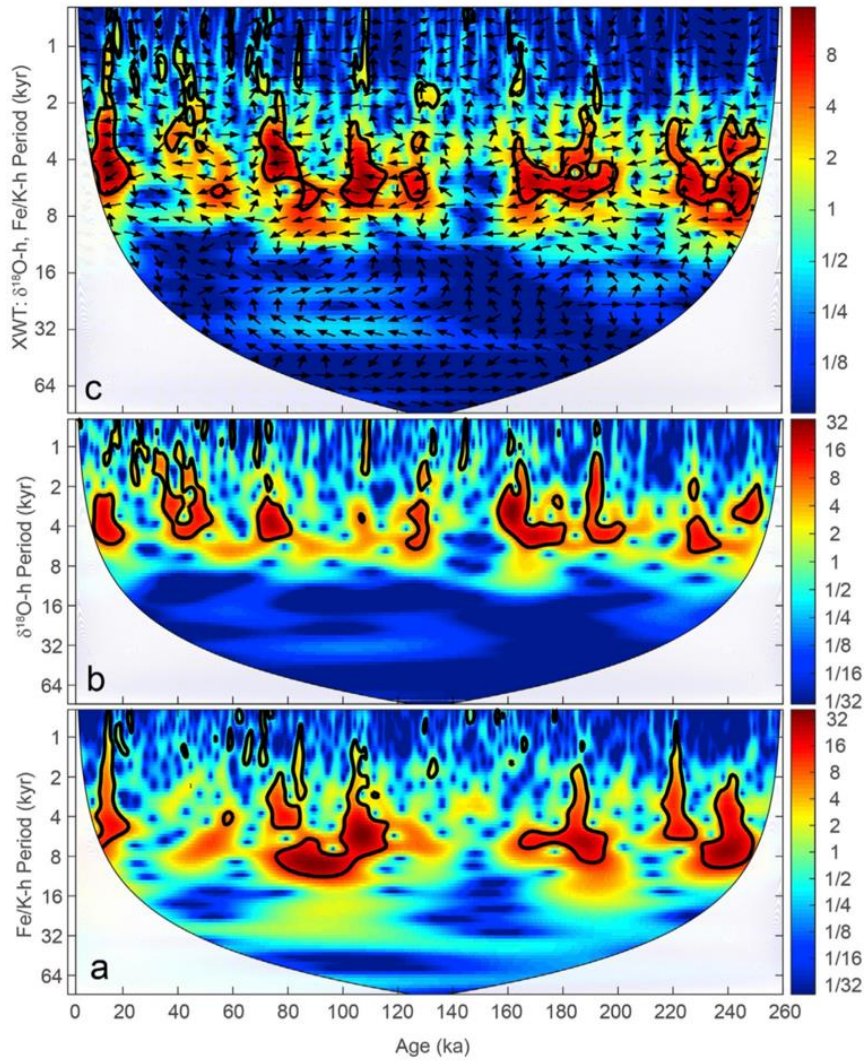


Figure 2. Continuous wavelet transforms (CWT) of Fe/K (a), speleothem $\delta^{18}\text{O}$ (b) and cross wavelet transform coherence (XWT) (c) between the two CWT. The 5% significance level against red noise is shown as a black contour. Arrows indicate the relative phase relationship with out-phase pointing to left and in-phase pointing to right.

9. 近 2000 年来 ENSO-SAM 对南极海冰范围数十年尺度上趋势的影响

翻译人：张亚南 zhangyn3@mail.sustech.edu.cn



Xavier Crosta, Johan Etourneau, Lisa C. Orme et al. *Multi-decadal trends in Antarctic sea-ice extent driven by ENSO–SAM over the last 2,000 years [J]. Nature Geoscience, 2021, 14, 156-160*
<https://doi.org/10.1038/s41561-021-00697-1>

摘要：过去 40 年里，尽管气候不断变暖，但南极海冰的范围却变得越来越广泛。这种趋势的区域表现与海洋热量的垂直再分配和大尺度风场变化有关。然而由于现代观测的时间较短，无法将这种趋势归因于人类活动或自然变化。作者提出了 2 个十年分辨率的海冰和海表温度记录，显示了 2000 年来南极印度洋海冰覆盖面积不均一性现象的普遍存在。该文的海洋记录在气候模型中的资料同化（data assimilation）表明重建出的不同区域环境条件结果是由数十年变率的厄尔尼诺—南方涛动和南半球环状模（Southern Annular Mode, SAM）所驱动。例如，在 El Niño/SAM 结合期间，从副热带到南大洋的热对流增加，向北输送的海冰减少。从而导致沿南极海岸的海冰被压缩，南极印度海区的海冰范围缩小。因此，作者的研究结果表明，南大洋的自然变化很大，并在该区域最近海冰变化的趋势上和其年代际变化中发挥了关键作用。

ABSTRACT: Antarctic sea ice has paradoxically become more extensive over the past four decades despite a warming climate. The regional expression of this trend has been linked to changes in vertical redistribution of ocean heat and large-scale wind-field shifts. However, the short length of modern observations has hindered attempts to attribute this trend to anthropogenic forcing or natural variability. Here, we present two new decadal-resolution records of sea ice and sea surface temperatures that document pervasive regional climate heterogeneity in Indian Antarctic sea-ice cover over the last 2,000 years. Data assimilation of our marine records in a climate model suggests that the reconstructed dichotomous regional conditions were driven by the multi-decadal variability of the El Niño Southern Oscillation and Southern Annular Mode (SAM). For example, during an El Niño/SAM– combination, the northward sea-ice transport was reduced while heat advection from

the subtropics to the Southern Ocean increased, which resulted in reduced sea-ice extent in the Indian sector as sea ice was compacted along the Antarctic coast. Our results therefore indicate that natural variability is large in the Southern Ocean and suggest that it has played a crucial role in the recent sea-ice trends and their decadal variability in this region.

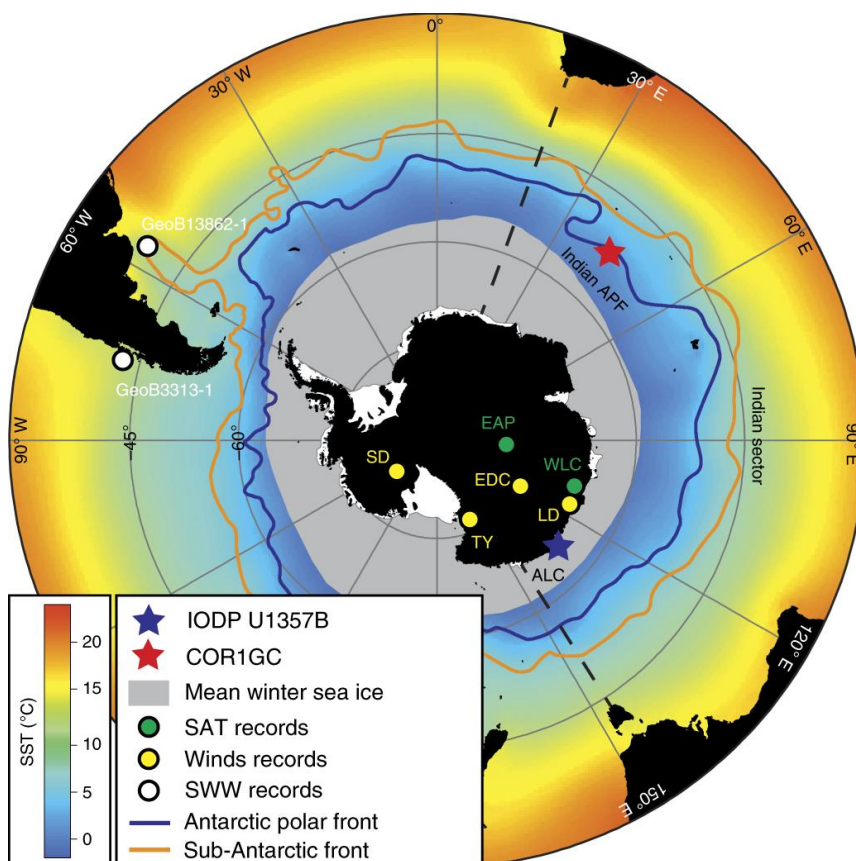


Figure 1. Location of studied marine cores and modern SO hydrographic features. IODP Hole U1357B site is shown by the blue star and COR1GC by the red star. The background map represents the modern (1955–2008) mean annual SST field from the World Ocean Atlas 2009 (<https://www.nodc.noaa.gov>). The modern mean locations of the sub-Antarctic Front (orange line) and APF (blue line). The modern mean winter sea-ice extent (grey shaded area). Green dots indicate the locations of the composite SAT reconstruction for the East Antarctic Plateau region (EAP) and the Wilkes Land coast area (WLC). Yellow dots show the locations of wind records reconstructed from the sodium records in Law Dome (LD), EPICA Dome C (EDC), Taylor Dome (TY) and Siple Dome (SD). White dots identify the locations of the westerly winds reconstructions inferred from the iron content in core GeoB3313-1 and from ice-volume-corrected *Globorotalia inflata* $\delta^{18}\text{O}$ values in core GeoB13862-1.

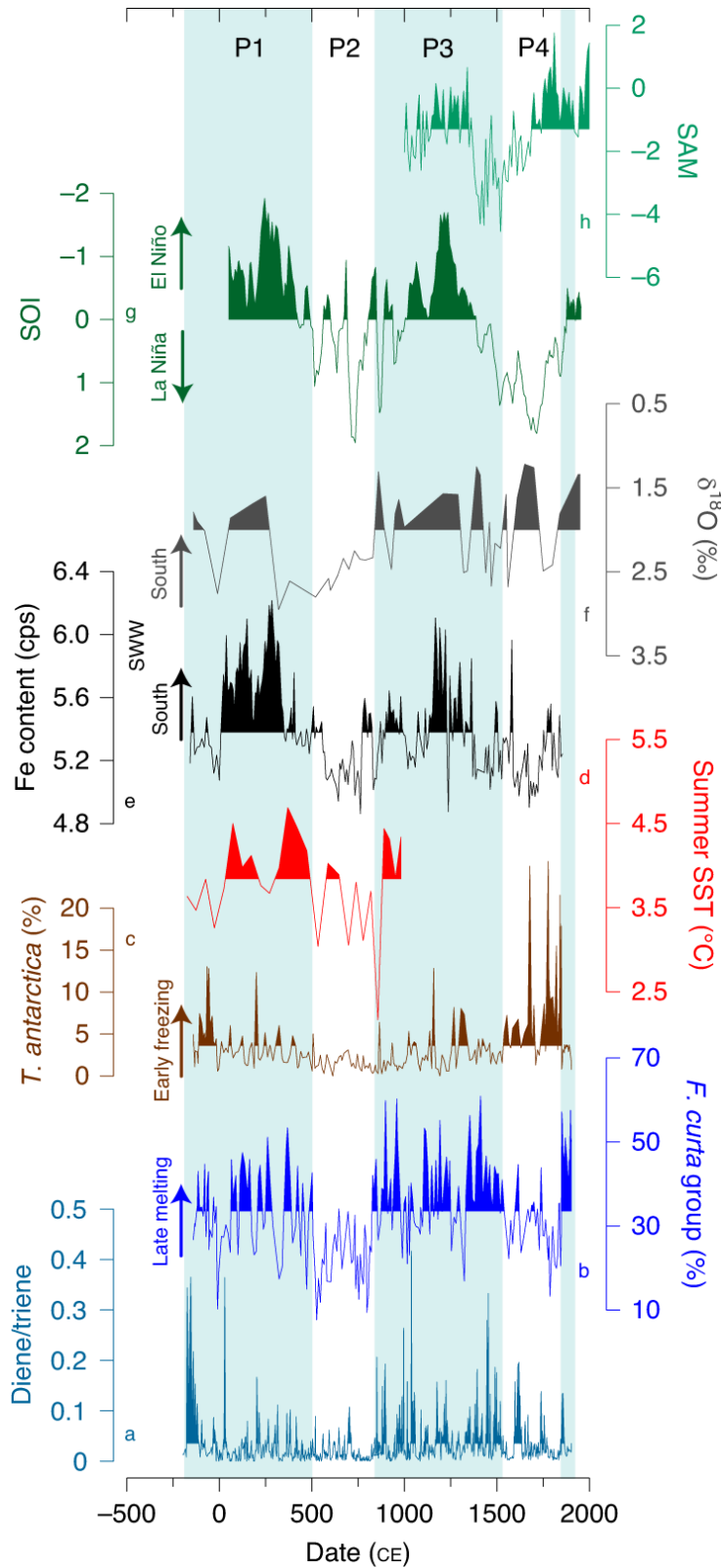
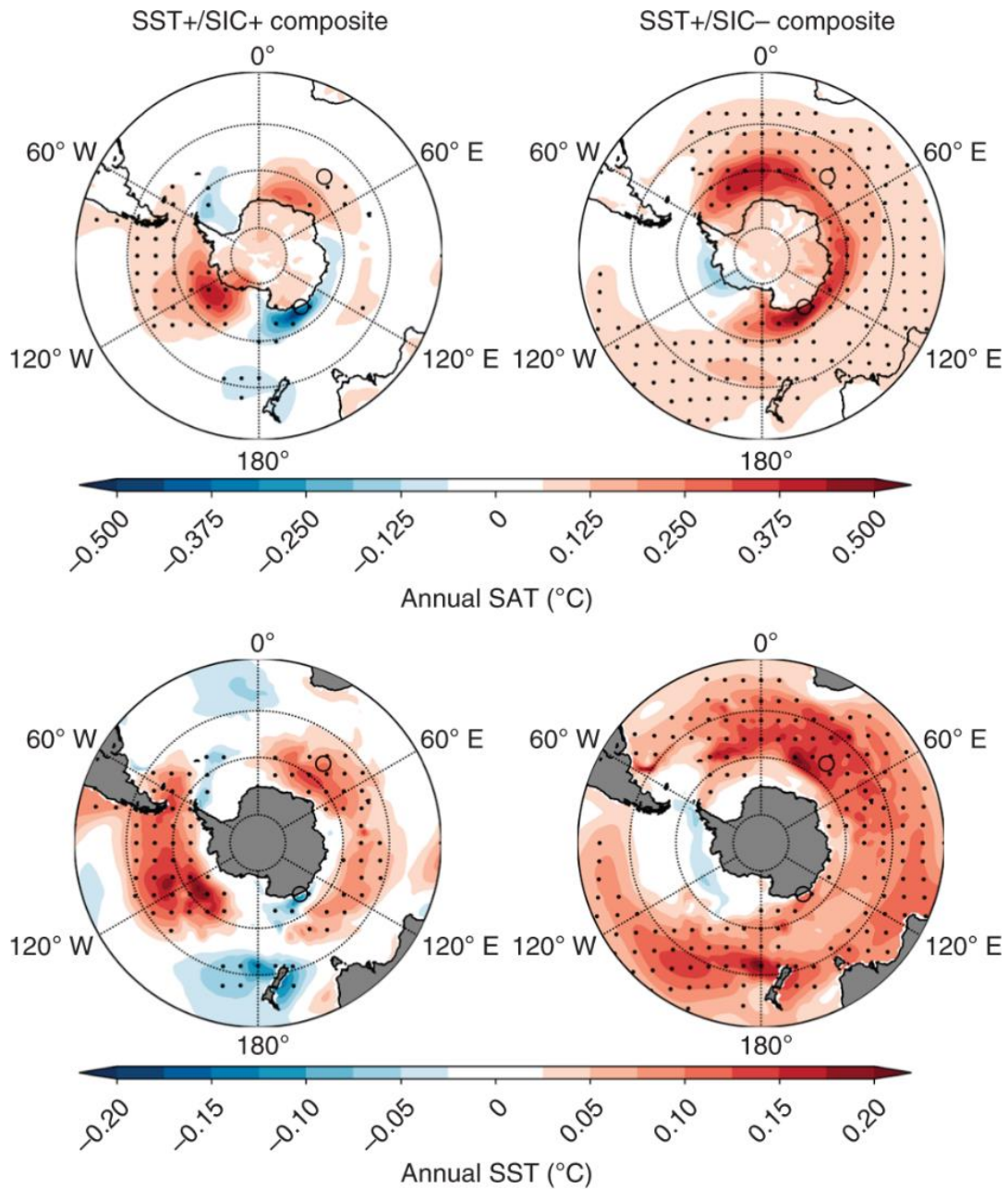


Figure 2. Intercomparison of sea-ice and climate records over the last 2,000 years. **a**, Diene/triene ratio in IODP Hole U1357B (this study). **b**, Relative abundances of the *F. curta* group in Hole U1357B (this study). **c**, Relative abundances of *Thalassiosira antarctica* in Hole U1357B core (this study). **d**, Mean summer SSTs estimated from diatom-based transfer function in COR1GC core (this study). **e**, Iron

content in GeoB3313-1 core with higher values indicating a poleward position of the southern westerly winds (SWW). **f**, Ice-volume-corrected *Globorotalia inflata* $\delta^{18}\text{O}$ record in GeoB13862-1 core, with lower values indicating meridional shifts of the Brazil–Malvinas Confluence and SWW. **g**, Southern Oscillation Index (SOI) record calculated as the difference between the reconstructed precipitation records from Indonesia and the Galapagos. **h**, Southern Annular Mode (SAM) record calculated from an array of temperature-sensitive proxy records in Antarctica and South America.



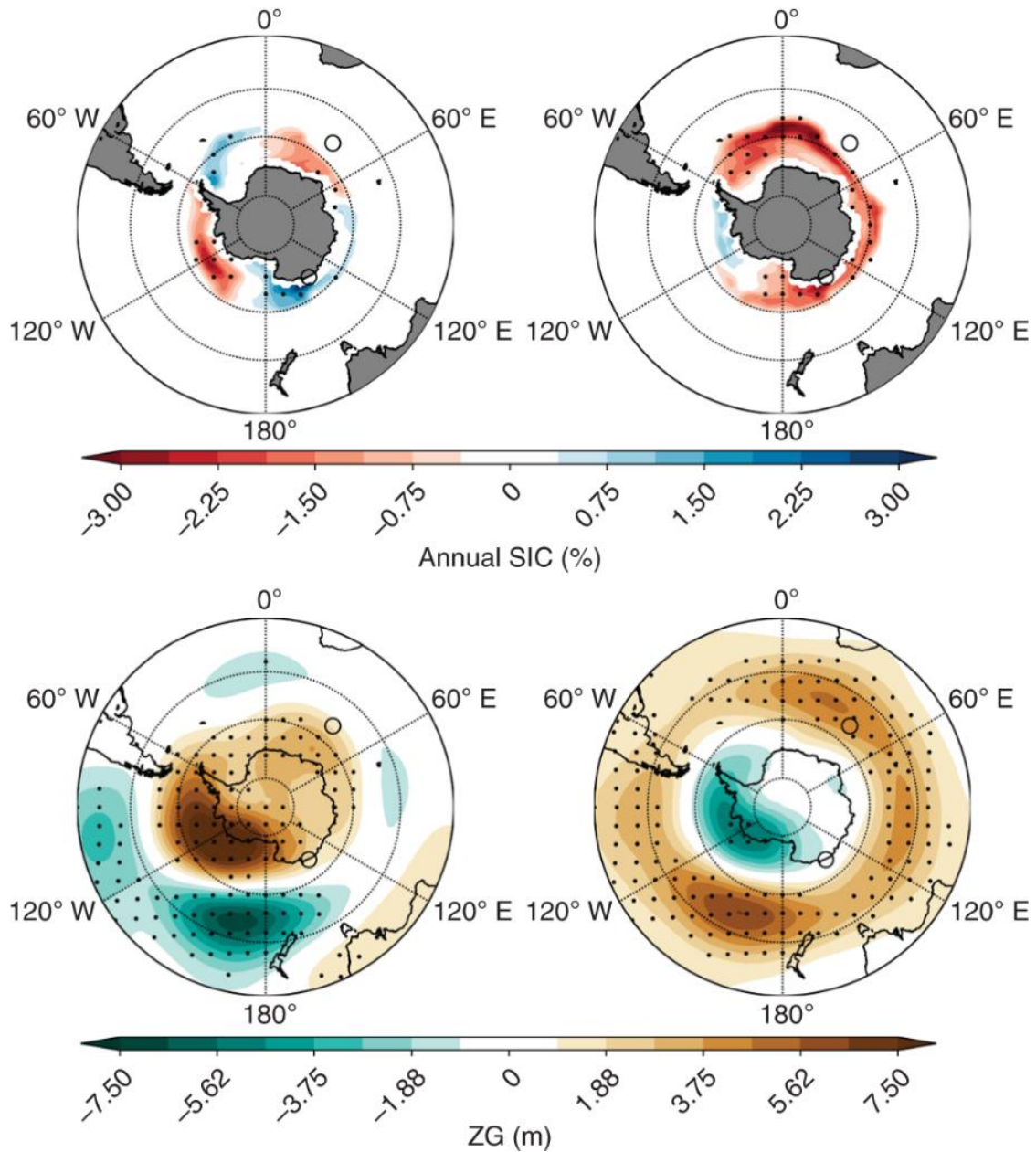


Figure 3. Mean environmental conditions for the SST+/SIC+ composite and the SST+/SIC- composite based on offline DA using the CESM1-CAM5 model outputs. Values represent anomalies to the first millennium (0–1000 CE) as reference. Circles represent the geographical locations of the two cores studied here (IODP Hole U1357B off Adélie Land and COR1GC around the Indian APF). ZG, geopotential height.

10. SCHA.DIF.4k:重建欧洲 4 kyr 以来的地磁场变化及其在测年中的应用

翻译人: 李海 12031330@mail.sustech.edu.cn



Pavón-Carrasco, F. J., Campuzano, S. A., Rivero-Montero, M., et al. SCHA.DIF.4k: 4000 years of paleomagnetic reconstruction for Europe and its application for dating [J]. Journal of Geophysical Research: Solid Earth, 2020, 126, e2020JB021237.

<https://doi.org/10.1029/2020JB021237>

摘要: 在欧洲考古地磁场模型 SCHA.DIF.3k 发布之后, 来自火成岩等材料的古地磁数据快速增加, 方向和古强度的数据分别增加了 90%和 180%。利用这一增长的优势, 作者提出了一个新的区域性地磁模型, 称之为 SCHA.DIF.4k, 该模型可用于模拟 4000 年以来欧洲大陆及其邻近区域的地磁场变化。为了模拟地磁场的偏角、倾角和强度, 作者在三次样条的时空基础上使用了区域 R-SCHA2D 法。在一个以北纬 40°N 和东经 10°E 为中心的 30°球面区域内选取合适的古地磁数据。此外, 为了更好的约束几个世纪以来地磁场的变化, 作者还引入了 HISTMAG 的历史数据。新的区域模型使我们能更好的定义欧洲的古磁场, 并且可以生成新的地磁长期变化曲线用于古地磁定年。利用这些曲线, 可以估算 4 kyr 以来的测年精度。正如预期的那样, 结果表明它很大程度上取决于数据的不确定性, 时间数据的分布以及地磁场本身的行为。此外, 相较于只使用方向数据, 使用全矢量地磁场数据, 可以提供更为精确的古地磁测年结果。

ABSTRACT: Since the publication of the European archeomagnetic field model SCHA.DIF.3k in 2009, the number of paleomagnetic data derived from archeological materials such as baked clays and volcanic rocks coming from Europe has increased by about 90% for directions and around 180% for intensities. Taking advantage of this increase, here we provide an updated regional archeomagnetic model, called SCHA.DIF.4k, for the European continent and adjacent areas and now covering the last four millennia. To model the three geomagnetic elements, declination, inclination and intensity, we use the regional R-SCHA2D technique in space and temporal basis of cubic splines. A critical selection of the archeomagnetic and volcanic data available in a spherical cap of 30° centered at 40° N latitude and 10° E longitude has been considered. In addition, in order to better constrain the behavior of the archeomagnetic field during the last centuries, we include the historical data of the HISTMAG compilation. The new regional model allows us to better define the paleomagnetic field over Europe as well as to generate new paleosecular variation curves for archeomagnetic dating purposes. Using these curves, the dating precision has been estimated for the

last 4 kyr. As expected, results show that it strongly depends on the data uncertainties, the temporal data distribution and the behaviour of the geomagnetic field itself. In addition, the use of the full vector geomagnetic field, instead of the directional information exclusively, provides more precise archeomagnetic dating results.

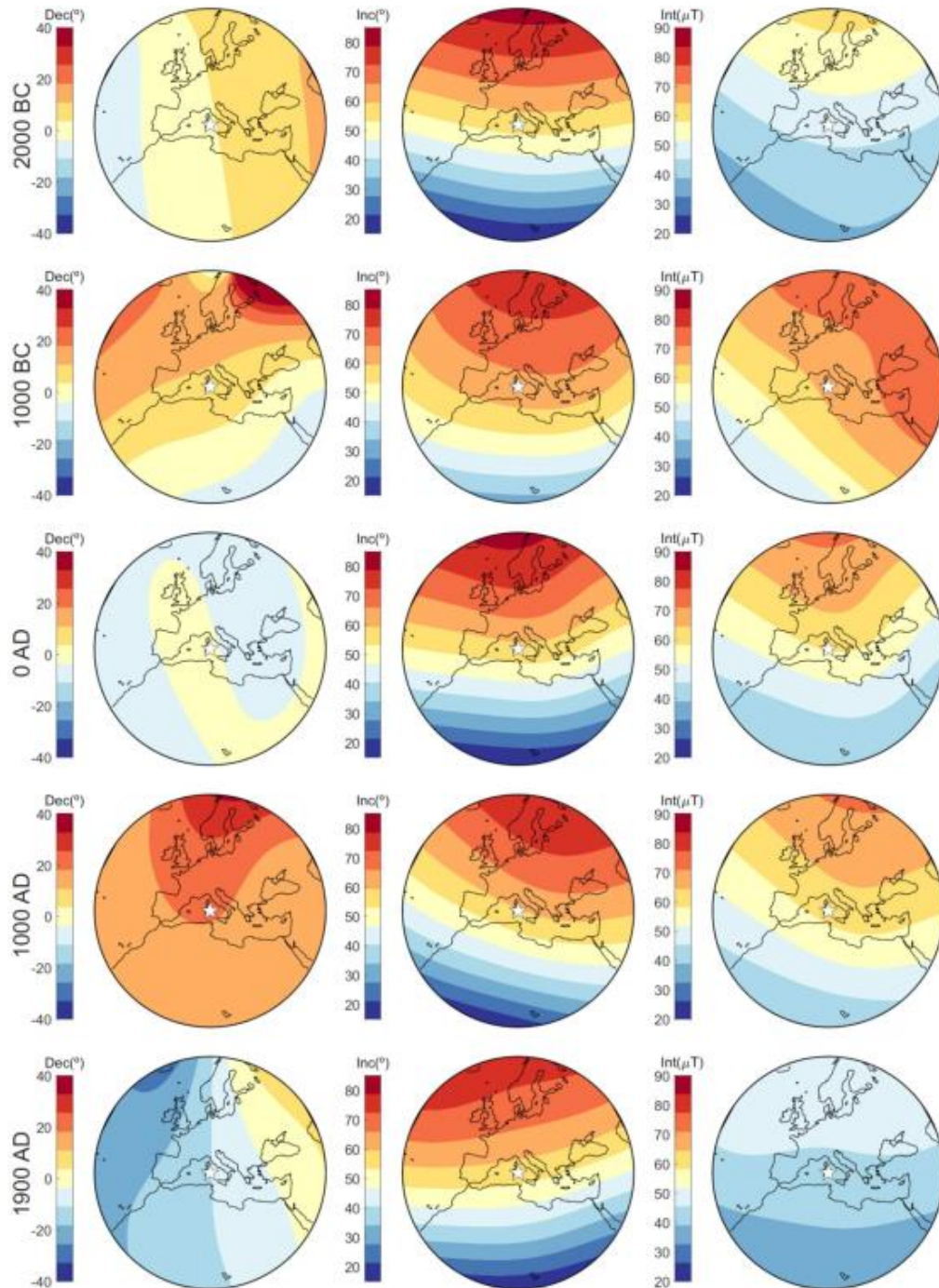


Figure 1. Declination (left), inclination (center), and intensity (right) maps by the SCHA.DIF.4k model. Maps at 2000 BC, 1000 BC, 0 AD, 1000 AD, and 1900 AD. The white star indicates the center of the spherical cap.

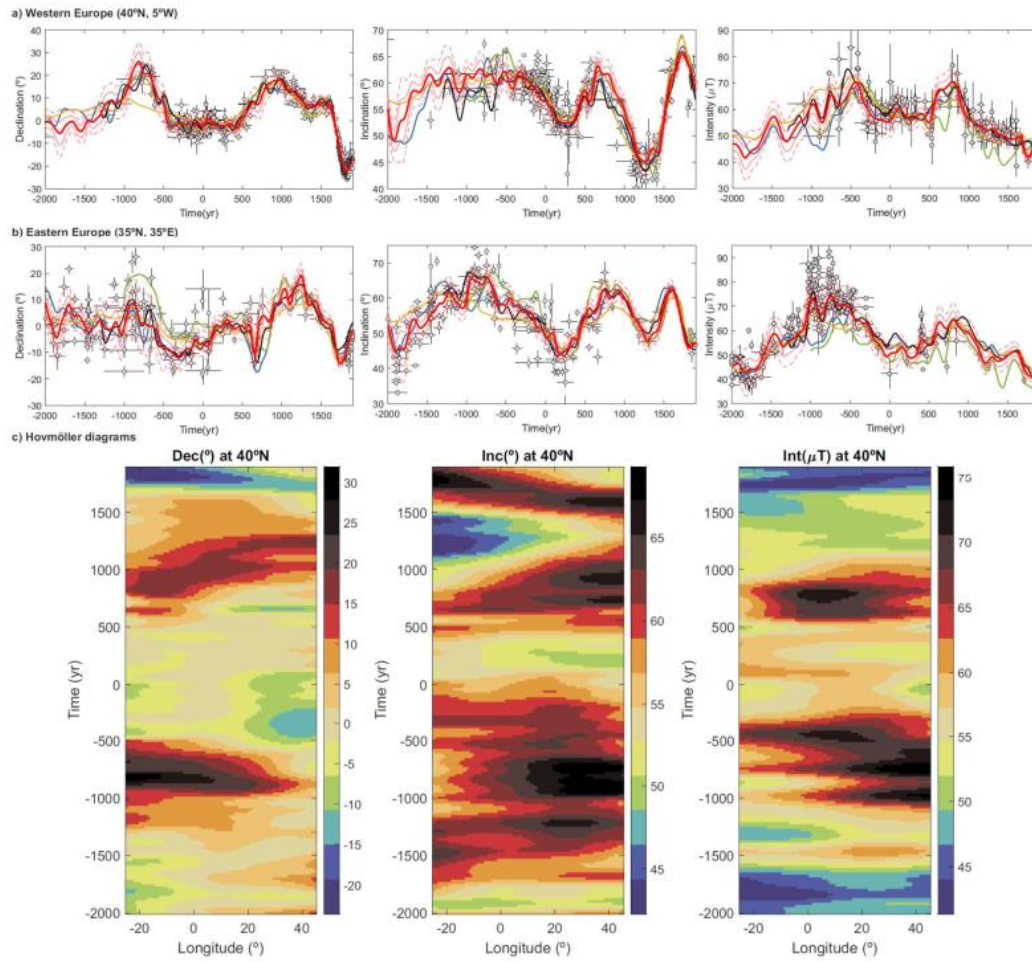


Figure 2. Paleosecular variation curves at a) 40 °N, 5 °W and b) 35 °N, 35 °E coordinates, and c) Hovmöller diagrams for the declination (left), inclination (center), and intensity (right) elements. For the paleosecular variation curves: red curves correspond to the new SCHA.DIF.4k model with error bands at 1σ (thin red lines) and 2σ (dashed red lines). Green curves represent the previous regional archeomagnetic model SCHA.DIF.3k. In addition, global archeomagnetic models CALSA10k.2 (yellow curves), SHA.DIF.14k (blue curves) and SHAWQ family (black curves) are also plotted. Archeomagnetic and historical data referred to each location are plotted for comparison as gray dots (with error bars). For the Hovmöller diagrams: they are calculated at a constant latitude of 40 °N for the range of longitudes inside the spherical cap

11. 茶马古道历史的社会韧性及其尺度效应



翻译人：郑威 11930589@mail.sustech.edu.cn

Yang L E, Chen J, Geng J, et al. *Social resilience and its scale effects along the historical Tea-Horse Road*[J]. *Environmental Research Letters*, 2021,16(4).

<https://doi.org/10.1088/1748-9326/abea35>

摘要：本研究采用实证分析的方法探讨中国西南茶马古道及其相关社区对重大自然灾害的社会韧性，以了解茶马古道及其相关社区长期保持和发展的方式。通过收集档案资料、文献再析、统计数据、监测数据和调查材料，对灾害影响和社会韧性进行定性和定量分析，为灾害影响和社会韧性的整体调查提供依据。结果表明：（1）自然灾害发生频繁但是有时空多样性并且造成的影响不同，为维持社会发展提供了多样化和有针对性的应对策略的可能；（2）强大的中央和地方治理持续改善基础设施和工业技术，以及与地方经验和灾害文化相结合的社会网络协作，是提高各级社会韧性的主要因素；（3）茶马古道地区在时空尺度上表现出不同的对自然灾害的社会韧性特征，多种社会韧性措施的结合使得整个社会系统长期在不同地区具有社会韧性。一般来说，长期尺度上看，具有多种反应能力的大型社会系统比小型系统和个体更具有社会韧性。研究重点表明，茶马古道地区虽然长期有频繁的自然灾害，但是社会经济、交通运输和先进技术总体保持了发展，并转变成为了更有韧性的状态。总体上，本文描述了茶马古道及其相关地区多种社会韧性措施的尺度效应，呼吁在多个时空尺度上对社会韧性和不同社会实体的转变进行研究。

ABSTRACT: This study adopted an empirical analysis to explore social resilience to major natural disasters along the Tea-Horse Road (THR) in southwest China and to understand why and how the THR and its connected communities maintained and developed over a long period. A set of archive data, literature re-analysis, statistical data, monitoring data, and surveyed materials were collected and qualitatively and quantitatively analyzed to support a holistic investigation of disaster impacts and social resilience. The results indicate that (1) natural disasters occurred frequently but were

distributed over place and time and had various impacts, which left possibilities for maintaining social development with diverse and specific coping strategies; (2) strong central and local governance continually improved infrastructure and engineering technologies, and collaboration in social networks with local experience and disaster cultures were the major contributing factors that enhanced social resilience at various levels; (3) the THR area demonstrated various features of social resilience to natural disasters in terms of spatial-temporal scales, where the combination of multiple resilience measures enabled the resilience of the entire social system at various places over long time periods. Generally, larger social systems with diverse response capabilities were more resilient than small and individual entities over a long time scale. The study highlights that the THR region withstood frequent natural disasters but maintained a general development of social economy, transportation, and advanced technologies, and performed a positive transformation to a more resilient status. Overall, this paper describes the scale effects of multiple resilience measures along the THR and calls for specific studies on social resilience and transformation of diverse social entities over multiple spatial-temporal scales.

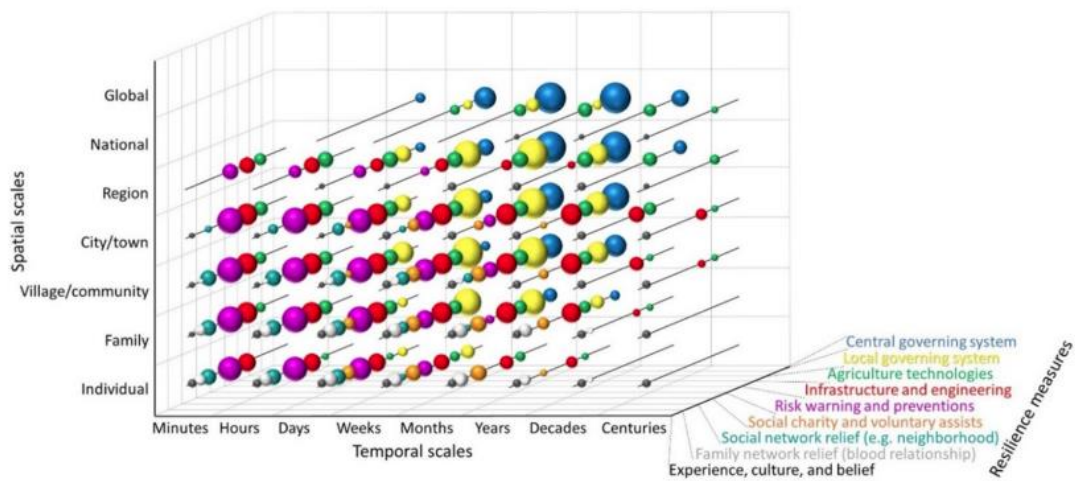


Figure 1. Conceptual illustration of the spatial–temporal scales and effects of various resilience measures. Bubble size indicates the relative effectiveness of each measure, which was based on empirical assessments.

12. 高温下磁铁矿、磁黄铁矿、赤铁矿的磁滞特征



翻译人：张伟杰 12031188@mail.sustech.edu.cn

Dunlop, David J. Magnetic hysteresis of magnetite, pyrrhotite and hematite at high temperature [J]. Geophysical Journal International 2021, 225(1): 1-14.

<https://doi.org/10.1093/gji/ggaa569>

摘要：含铁矿物在高于环境温度下的磁性不仅控制着它们在地球和其他行星深处的磁性表达，还控制着它们被带到地表冷却过程中获得的热剩磁或热化学剩磁。本文报道了天然磁黄铁矿和赤铁矿以及天然和合成的各种尺寸磁铁矿组合在居里点以下的磁滞参数的测量结果。由饱和剩磁 M_{rs} 与饱和磁化 M_s 的比值可以推断出畴结构的变化。在几乎所有被研究的磁铁矿和磁黄铁矿， M_{rs} 相比于 M_s 随着测量温度的升高下降地更快，表明单畴颗粒的热解阻或 vortex 形成，多畴晶粒在高温时畴壁的增加或再活化。矫顽力 H_c 是剩磁相对于变化后的磁场的稳定性的一种测量，它也随着测量温度的增加而减小，其速率通常与 M_{rs} 相似，但在居里点附近通常保持一个有限值。

ABSTRACT: The magnetic properties of iron-bearing minerals at above-ambient temperatures control their magnetic expression at depth in the Earth and other planets, as well as the permanent memory they retain as thermoremanence or thermochemical remanence when brought to the surface and cooled. This paper reports magnetic hysteresis parameters measured at temperatures up to the Curie point T_C for natural pyrrhotite and hematite and for suites of sized magnetites, both natural and synthesized. Domain structure changes can be inferred from the ratio of saturation remanence M_{rs} to saturation magnetization M_s . In almost all magnetites and pyrrhotites studied, M_{rs} decreases more rapidly with increasing measurement temperature T than M_s , indicating thermal unblocking or vortex development in single-domain grains and addition or remobilization of domain walls at high T in multidomain grains. During cooling of a rock, iron minerals might then denucleate domains or vortices. Coercive force H_c , a measure of stability against changing magnetic fields, also decreases with increasing measurement T , usually at a rate similar to that of M_{rs} , but often retains a finite value near the Curie point.

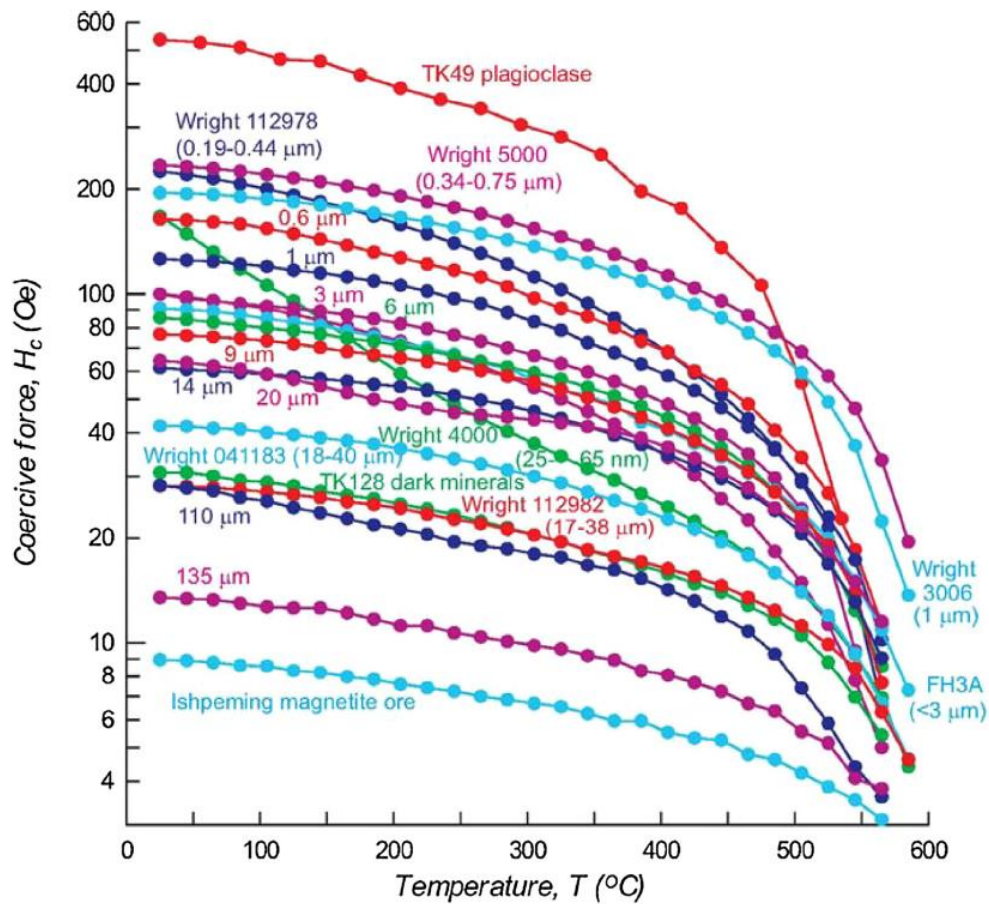


Figure 1. H_c versus T data for all magnetite samples plotted on a logarithmic scale. Apart from the more rapid decreases, the patterns are the same as in Fig. 4. TK49 and Wright 112978 and 4000 have cross-cutting trends resulting from reduction of H_c by thermal activation. The 20 μm and pre-annealed 3 μm magnetites have aberrant/cross-cutting trends. The largest MD grains (135 μm and Ishpeming ore) have gently descending $H_c(T)$ data with no sign of thermal activation even above 500 $^\circ\text{C}$. The other 13 samples have subparallel $H_c(T)$ trends with steady descents and steeper plunges above 500 $^\circ\text{C}$ marking ultimate unblocking of all remanence carriers. Note on units: 1 Oe = 79.6 A m $^{-1}$; the equivalent B is 10 $^{-4}$ T.

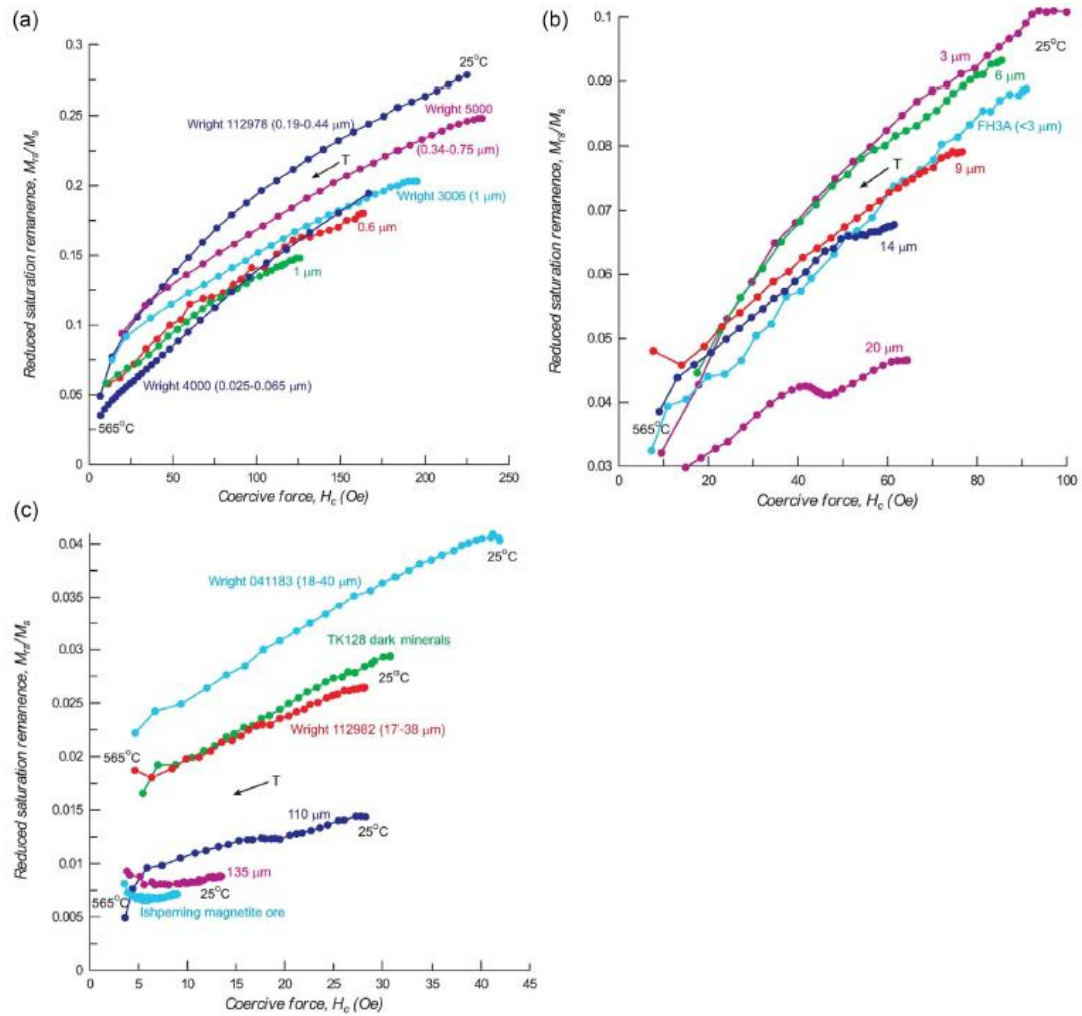


Figure 2. Temperature evolution of M_r/M_s and H_c data (squareness-coercivity plots). (a) Data for grain sizes $\leq 1 \mu\text{m}$. Curves for Wright 5000, Wright 3006, 0.6 μm and 1 μm magnetites form a nested set. Wright 112978 and Wright 4000 contain thermally activated fine SD grains whose more rapidly decreasing M_r/M_s and $H_c(T)$ data cut across the other trends. (b) Data for PSD sizes (3–20 μm). The 3 and 6 μm data form a set, as do the 9 and 14 μm data. Both are cross-cut by the data of FH3A, which has a broad size spectrum. The 20 μm data are clearly anomalous. (c) Data for small MD (TK128 and Wright 041183 and 112982) and large MD (110 and 135 μm and Ishpeming ore) grains. The slopes of the quasi-linear plots level out as grain size increases but in all cases H_c changes much more rapidly with T than M_r/M_s . Note on units: 1 Oe = 79.6 A m⁻¹; the equivalent B is 10⁻⁴ T.

13. 赤道太平洋 E-O 转换期间生产力变化



翻译人：王敦繁 dunfan_w@foxmail.com

Moore, T. C., Jr., B. S. Wade, T. Westerhold, et al. *Equatorial Pacific productivity changes near the Eocene-Oligocene boundary [J].* *Paleoceanography*, 2014, 29, 825–844,

<https://doi.org/10.1002/2014PA002656>.

摘要：人们普遍认为，始新世晚期高纬度地区的生产力有所增加，渐新世早期仍保持在较高水平。在赤道始新世-渐新世过渡时期(EOT)，生产力增加或减少的证据已经提出，但通常只基于一种古生产力指标，而且往往是在 EOT 本身恢复不完全的地点。本研究在东赤道太平洋的三个钻探点(ODP 1218 和 IODP U1333 和 U1334)获得了始新世-渐新世过渡的完整记录。在这些站位检测到的四个古生产力指标，以及对早渐新世浮游有孔虫的碳和氧同位素测量，为这一重要气候跨越边界的海洋生态变化提供了证据。输出生产力在渐新世刚开始(~33.7 Ma)急剧下降，几十万年后才恢复；然而，渐新世早期的整体古生产力从未达到始新世晚期和更现代时期的平均水平。深海和浅层浮游有孔虫同位素梯度的变化表明，在渐新世早期，温跃层逐渐浅化，影响了重晶石、底栖有孔虫和蛋白石的累积速率，以及 33.5 Ma 附近的硅藻丰度。从 33.3 Ma 开始，大量的大型硅藻表明了一个中等的温跃层深度，随后是进一步的浅滩化，导致较小的硅藻占主导地位，根据底栖有孔虫的积累速率推断该时期海洋初级生产力有所增加。

ABSTRACT: There is general agreement that productivity in high latitudes increased in the late Eocene and remained high in the early Oligocene. Evidence for both increased and decreased productivity across the Eocene-Oligocene transition (EOT) in the tropics has been presented, usually based on only one paleoproductivity proxy and often in sites with incomplete recovery of the EOT itself. A complete record of the Eocene-Oligocene transition was obtained at three drill sites in the eastern equatorial Pacific Ocean (ODP Site 1218 and IODP Sites U1333 and U1334). Four paleoproductivity proxies that have been examined at these sites, together with carbon and oxygen isotope measurements on early Oligocene planktonic foraminifera, give evidence of ecologic and oceanographic change across this climatically important boundary. Export productivity dropped

sharply in the basal Oligocene (~33.7 Ma) and only recovered several hundred thousand years later; however, overall paleoproductivity in the early Oligocene never reached the average levels found in the late Eocene and in more modern times. Changes in the isotopic gradients between deep- and shallow-living planktonic foraminifera suggest a gradual shoaling of the thermocline through the early Oligocene that, on average, affected accumulation rates of barite, benthic foraminifera, and opal, as well as diatom abundance near 33.5 Ma. An interval with abundant large diatoms beginning at 33.3 Ma suggests an intermediate thermocline depth, which was followed by further shoaling, a dominance of smaller diatoms, and an increase in average primary productivity as estimated from accumulation rates of benthic foraminifera.

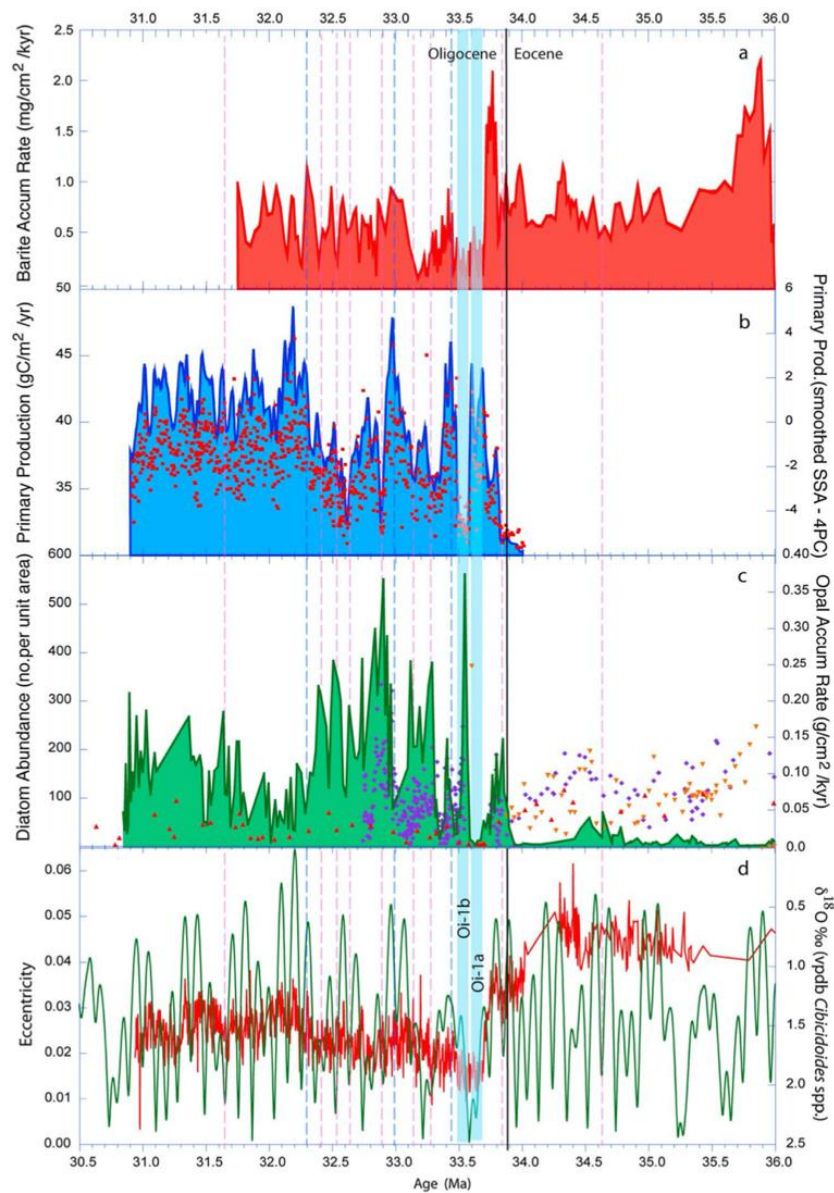


Figure 1: Proxy measurements for paleoproductivity. (a) Barite accumulation rates, proxy for export productivity measured in Site U1333 (corrected from Erhardt et al. [2013]): red-filled curve. (b) Blue curve and red squares, estimates of primary productivity [Herguera and Berger, 1991] based on benthic foraminifera (>150 μm) accumulation rate in Site 1218 (corrected from Coxall and Wilson [2011]). Red squares are individual sample estimates (see Table S2). Blue curve, sample data smoothed using single spectrum analysis [Paillard et al., 1996] with four principal components. (c) Diatom abundance measured in 100 fields of view (see text) on strewn (settled) slide samples, proxy for export productivity from Site U1334 [Baldauf, 2013]: green-filled curve. Opal accumulation rates measured in Site 1218, proxy for export productivity: blue triangles from Vanden Berg and Jarrard [2004] as adjusted by Moore et al. [2008], orange inverted triangles from Lyle et al. [2005], and red triangles from this study. (d) Red curve: oxygen isotopes measured on benthic foraminifera [Coxall and Wilson, 2011]; green curve: orbital eccentricity [Laskar et al., 2011]. Vertical dashed lines illustrate positive relationship between BAR, primary productivity, and high eccentricity (blue) and positive relationship between diatom abundance, opal MAR, and low eccentricity (red). All data plotted versus age (Ma) [Westerhold et al., 2014]. Light blue vertical bars indicate glacial intervals Oi-1a and Oi-1b. Vertical black line indicates Eocene-Oligocene boundary [Westerhold et al., 2014].